ROYAL SOCIETY
OF CHEMISTRY

REVIEW ARTICLE

Check for updates

A guide for the characterization of organic electrochemical transistors and channel materials

David Ohayon,† Victor Druet† and Sahika Inal (iD) *

The organic electrochemical transistor (OECT) is one of the most versatile devices within the bioelectronics toolbox, with its compatibility with aqueous media and the ability to transduce and amplify ionic and biological signals into an electronic output. The OECT operation relies on the mixed (ionic and electronic charge) conduction properties of the material in its channel. With the increased popularity of OECTs in bioelectronics applications and to benchmark mixed conduction properties of channel materials, the characterization methods have broadened somewhat heterogeneously. We intend this review to be a guide for the characterization methods of the OECT and the channel materials used. Our review is composed of two main sections. First, we review techniques to fabricate the OECT, introduce different form factors and configurations, and describe the device operation principle. We then discuss the OECT performance figures of merit and detail the experimental procedures to obtain these characteristics. In the second section, we shed light on the characterization of mixed transport properties of channel materials and describe how to assess films' interactions with aqueous electrolytes. In particular, we introduce experimental methods to monitor ion motion and diffusion, charge carrier mobility, and water uptake in the films. We also discuss a few theoretical models describing ion–polymer interactions. We hope that the guidelines we bring together in this review will help researchers perform a more comprehensive and consistent comparison of new materials and device designs, and they will be used to identify advances and opportunities to improve the device performance, progressing the field of organic bioelectronics.

King Abdullah University of Science and Technology (KAUST), Biological and Environmental Science and Engineering Division, Organic Bioelectronics Laboratory, Thuwal 23955-6900, Saudi Arabia. E-mail: sahika.inal@kaust.edu.sa

† These authors contributed equally.

David Ohayon is a Postdoctoral Fellow in the Organic Bio-electronics group at King Abdullah University of Science and Technology (KAUST). He received his MSc and BSc degrees in chemistry and physics from the Graduate School of Chemistry, Biology, and Physics of Bordeaux in France in 2016. He completed his PhD degree in Bioscience at KAUST in 2020, focusing on the development of n-type conjugated polymers for point-of-care applications. His research interests cover advanced and functional materials for early, rapid and accurate disease and pathologies diagnosis, (bio)actuating purposes, and the development of biomedical devices.

David Ohayon

Victor Druet is a PhD candidate in the Organic Bioelectronics group at KAUST. He received his MSc and BSc degrees in chemistry and physics from the Graduate School of Chemistry, Biology, and Physics of Bordeaux in France in 2018, with a major in nano and micro technology. His research focuses on the development of biosensors relying on n-type organic semi-conductors and understanding their operation mechanisms.

Victor Druet

This journal is © The Royal Society of Chemistry 2023

*Chem. Soc. Rev.*, 2023, **52**, 1001–1023 | **1001**

1. Introduction

Organic bioelectronics develops electronic devices that interface living systems through organic electronic materials. These devices detect diverse pathologies and regulate the physiology and processes of individual cells, tissues, and organs. One popular bioelectronic device is the organic electrochemical transistor (OECT), which has been used in applications ranging from biosensors to neuromorphic computing and in fundamental studies that benchmark mixed (ionic and electronic) conduction properties of materials.[1,2] The OECT operates like a switch, in which the electrochemical state and impedance of the gate electrode control the amount of current flowing in the channel, which is connected to the gate electrode through an electrolyte. OECTs convert ionic fluxes in the electrolyte into electronic signals and during ionic-to-electronic signal conversion, the ionic signals are also amplified, a property intrinsic to the transistor circuitry. Therefore, especially for biosensing, with their efficient transduction and large amplification, OECTs have become a valuable tool. A high amplification performance and fast-switching of the channel's conductivity guarantee the detection of weak biological signals occurring at various speeds. Research on the development of new materials for OECTs and optimization of device geometry has thus primarily focused on enhancing these two parameters.

While high amplification is the distinguishing property of OECTs, other features render their use at the biological interface compelling. First, OECTs generally use aqueous electrolytes, which are intrinsically compatible with biological media. Second, the device fabrication is easy, versatile, and compatible with various substrates. Third, the gate electrode and the channel can be placed in different positions, allowing the construction of devices with various form factors. Lastly, a broad range of materials or electrolytes can be integrated into these devices, and different geometries are feasible. These features enable a diverse set of applications. For instance, OECTs fabricated on conformable substrates were implanted on the cortex and mapped electrocorticography signals over a large surface, achieving a higher spatial resolution and signal-to-noise ratio (SNR) than conventional electrodes.[3,4] An implantable OECT array detected nanomolar concentrations of catecholamine, a key neurotransmitter regulating neural functions, while the device operated for hours at half of the conventionally required voltages.[5] Oxidase enzyme integrated OECTs quantified minute changes of lactate,[6] glucose,[7] or cholesterol[8] concentrations in various media including saliva,[9] sweat,[10] cell culture media,[11] and sap of a tree stem.[12] When these devices were integrated with microfluidic channels, fluid flow rate could be controlled and a lower detection limit was achieved in small sample volumes.[13] When functionalized with biochemical moieties, OECTs detected binding events of pathogens or the antibodies raised against them.[14,15] Culturing cells into a transwell placed between the channel and the gate electrode[16] or directly onto the OECT channel[17] enabled monitoring of cell barrier integrity, rendering real-time drug screening possible without the need for optical labels.[18] The OECT detected the activity of ion channels tethered onto supported lipid membranes, which is essential for identifying pathologies and potential cures.[19,20] Solid gel electrolytes permitted the fabrication of all-solid-state OECTs to realize ultrasensitive pressure sensors where physical contact modulated the ionic doping mechanism in the channel.[21] While the range of OECT applications is broad, the evaluation of OECT performance must be universal, but is hard to achieve due to the interdisciplinary nature of the research. Using standard techniques and guidelines for device performance evaluation can help the field to progress further and may lead to commercial applications.

Besides the influence of structural parameters (such as channel geometry, gate electrode type, electrolyte concentration, *etc.*), the channel material properties dictate the OECT performance. Many OECTs comprise soft, π-conjugated polymers or small molecules in the channel with the ability of mixed charge transport (named as mixed ionic and electronic conductors, *i.e.*, OMIEC).[22,23] The ideal channel material displays efficient electronic transport while facilitating ion uptake, release, and transport, two events that are coupled and require conflicting film morphologies.[24,25] Studies so far have aimed to maximize the number of ions that the OMIEC film can take, which is associated with the volumetric capacitance, and the transport speed of the electronic charges that the ions compensate for. Synthetic strategies have made longer chains with stiff backbones to improve charge transport and removed the contribution of ionic components in the film to enhance the electronic charge density.[26–28] Postprocessing efforts (such as side chains removal,[29] annealing,[30] acid post-treatment,[31] solvent mixtures[32,33] or small molecule additives in the solution[34,35]) aimed to improve chain aggregation,[25] reduce traps,[36] increase the charge carrier density or introduce chemically doped charges in the film.[37] All these efforts have focused on OECT amplification performance. Besides amplification, the switching speed is also important for biological applications,
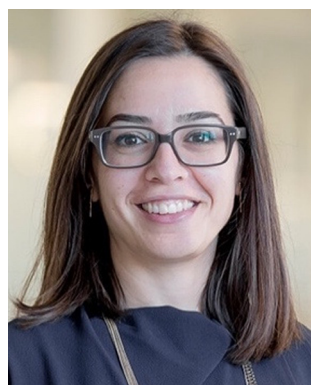
Sahika Inal is an Associate Professor of Bioengineering at KAUST and has been leading the Organic Bioelectronics group since 2016. She received her MSc in Polymer Science (2009) and PhD in Experimental Physics (2013) from the University of Potsdam (Potsdam, Germany). She was a post-doctoral fellow in the Department of Bioelectronics at the Centre Microelectronique de Provence in France, designing electronic ion pumps and scaffolds.

Sahika Inal

Her group at KAUST investigates ion/electron conduction in organic electronic materials and designs bioelectronic devices that can sense and actuate biological signals.

1002 | *Chem. Soc. Rev.*, 2023, **52**, 1001–1023

This journal is © The Royal Society of Chemistry 2023

regulated by the channel material. If the transistor does not switch ON or OFF within the duration of a biological event, *i.e.*, neurons firing or a chemical binding reaction, the device will be insensitive to it. Any barrier against ion penetration and release will slow volumetric charging, which can be monitored by techniques that track ion transport inside the film. In addition, studies showed the importance of water uptake by the channel,[38] highlighting that excessive swelling with water may disrupt electronic charge transport, slowing the OECT, and causing poor reversibility.[30,39,40] In all these efforts, it is crucial to monitor and control ion transport and swelling in the channel and study material properties using universal techniques to understand materials chemistry-materials properties-device performance relationships.

Although the OECT has been widely adopted, the field has yet to set a universal consensus on reporting device performance and materials figures of merits. In this review, we first discuss different OECT configurations and commonly used fabrication techniques. We introduce the operation principle of devices and describe the methods used to evaluate the steady-state and the transient characteristics and the

conditions that need to be considered for performance metrics reporting. We then examine how the figures of merit of OECT materials have been determined and the experimental techniques reported for such analysis. This review aims to present a standardized material when assessing the mixed conductivity of OMIECs and gives insight into the characterization methods used for OECT performance evaluation.

2. OECT architecture and characterization

2.1. Configuration and fabrication

Fig. 1 A shows a schematic for a common OECT architecture with various components. The OECT comprises an OMIEC thin film in the channel, bridging the source and drain electrodes. The third terminal of the device is the gate electrode, which can be an unpolarizable electrode, the most popular one being the Ag/AgCl electrode, or a polarizable metal electrode (Pt, Au). The metal gates can be further coated with an OMIEC film. The gate electrode may contain biomolecules or other functional
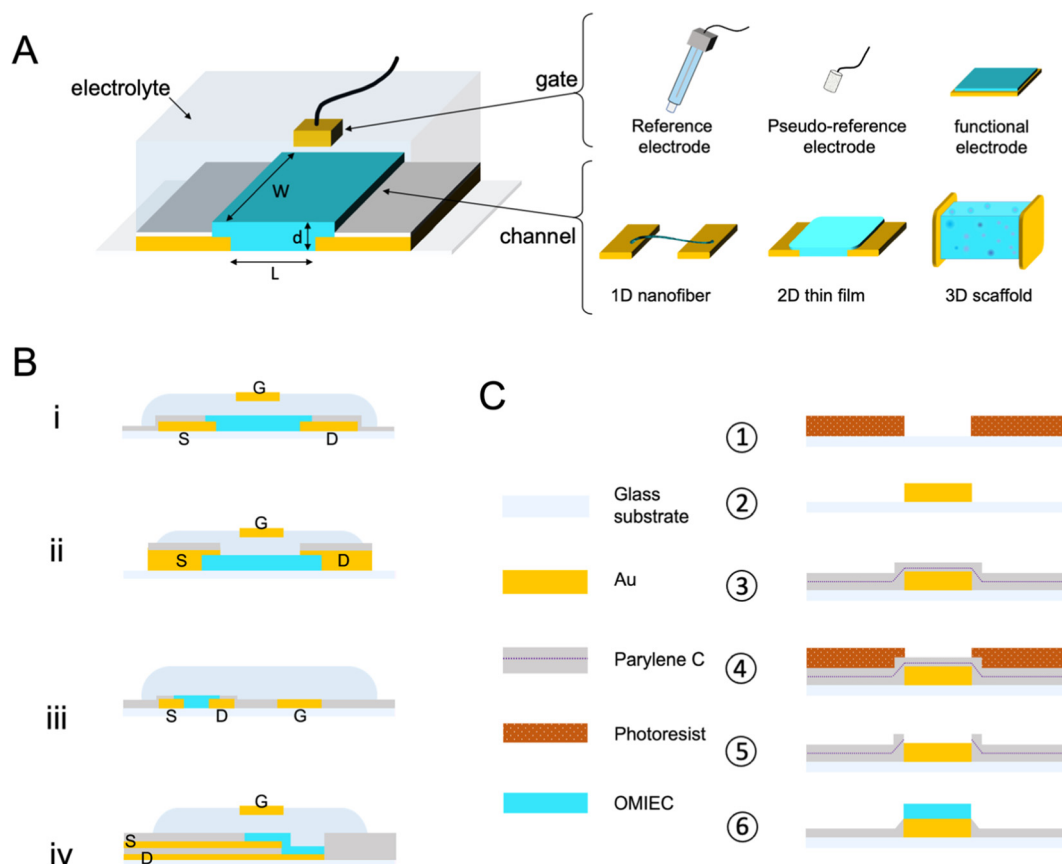

Fig. 1 OECT architecture and fabrication. (A) The schematic represents the typical architecture of an OECT with an OMIEC film cast between the source and the drain electrodes with channel dimensions: length (L), width (W), and thickness (d). The gate electrode can be an Ag/AgCl reference electrode, a pseudo-reference electrode, or any other material, including conducting polymers, metals, or metal oxides. The OMIEC channel can be processed as a 1D fiber, a 2D-thin film, or a 3D scaffold. (B) The most common OECT architectures are bottom contact (i), top contact (ii), coplanar (iii), and vertical (iv). (C) Basic steps involved in photolithography for the microfabrication of OECT: photoresist patterning (1), Au deposition and photoresist removal (2), two layers of PaC vaporization separated by an anti-adhesive layer (3), second photoresist patterning (4), dry etching and photoresist removal (5), OMIEC coating and PaC peel-off (6).

This journal is © The Royal Society of Chemistry 2023

Chem. Soc. Rev., 2023, **52**, 1001–1023 | **1003**

materials. For instance, titanium particles can be immobilized on an Au gate for applications requiring light sensitivity.[41–43] 2D materials or nanomaterials such as graphene or gold nanoparticles can be added to the gate electrode surface to increase the electrochemically active surface area or electrochemical reactivity to a particular chemical species.[41,44,45] OECTs use an electrolyte that has an interface with both the gate electrode and the channel. The electrolyte contains salt ions and can be in the form of a simple liquid,[46] more complex biological fluid (saliva,[9] sweat,[10] cell culture medium,[11] cerebrospinal fluid,[47,48] etc.), a hydrogel,[49] or an ionic liquid. Ionic liquids are particularly interesting as their low vapor pressure makes them non-volatile, ideal for wearable applications which seek long-term recording performance and high SNR.[50] They demonstrate high ionic conductivity while granting a wider electrochemical window than the water-based electrolyte. The gate electrode can be dipped into the aqueous, gel, or ionic liquid type electrolyte, or coated on top of the electrolytes with low fluidity. It can as well be placed on the same plane as the channel. This spatial freedom gives rise to various OECT architectures answering specific applications' needs. The parts of the source and drain electrodes that are not in contact with the channel are insulated. These electrodes are extended on the substrate to establish the electronic connection with the source measure unit (SMU). The source and drain electrodes can interface from below (Fig. 1B-i) (if they are patterned before the channel material) or from above (Fig. 1B-ii). Bottom contacts represent most devices produced to date and possess a faster switching speed than their top contact counterparts; nonetheless, it has been shown that positioning the contact above the channel would promote higher reproducibility of devices.[51] A significant drawback of the top contact configuration lies in its interface with the electrolyte, which can lead to parasitic reactions. Such reactions cause a high leakage current. Using electrochemically inert materials limits the occurrence of these parasitic reactions.[52] The two designs use an out-of-plane gate dipped into the electrolyte above the channel, a very suitable architecture for benchtop experiments. Yet, the coplanar gate configuration, where the channel and gate are fabricated on the same substrate (Fig. 1B-iii), is more practical as the user does not have to handle two separate components. The coplanarity renders possible, for instance, OECTs fabricated on one shank[48] or as a wearable patch.[53] A fourth and most recent architecture is the vertical OECT, where the source and drain contacts are stacked on top of each other and separated by an insulating layer, forming a vertical OMIEC channel (Fig. 1B-iv). This design permits a smaller device footprint, a crucial parameter for in vivo applications, and a reduced channel length which benefits both the transconductance and the device switching speed.[52,54] One often overlooked parameter when designing an OECT is the overlap between the OMIEC and the metal contact. While the overlap size does not affect the steady-state performance of the OECT, it increases the response time, measured as a lower cut-off frequency with increasing overlap.[55] Generating a clean contact where the OMIEC completely wets the metal is critical to ensure

good device characteristics. Using self-assembled monolayers has been shown to improve the interface quality between the two materials, leading to higher steady-state performance.[56]

Micron-scale OECT channels are commonly fabricated using photolithography which involves multiple steps in a cleanroom facility. Such dimensions are necessary for applications where the area that the array interfaces have to be minimized, and when high spatial resolution is required. Single-cell recordings, for instance, would be possible if the size of the device matches that of the cell. Fig. 1C summarizes the key steps used in this photolithographic fabrication of OECTs. First, the metal contacts (source, drain, and gate often made of chromium/gold) are deposited on the substrate through photoresist-assisted patterning. An insulating layer, often parylene C (PaC), is vaporized over the wafer, followed by a dry etching procedure to open the channels (and the gate contacts). A second thicker layer of the insulator is then coated, including an anti-adhesive layer underneath; it is etched and peeled off after coating the OMIEC material. Except when using top contact configuration, the OECT (micro)fabrication precedes the coating of the active organic material onto the channel (and sometimes the gate too). The type of coating procedure can take many forms thanks to the versatile processability of the OMIEC. This procedure can supply high-performing devices with a critical dimension (the channel length) of only a few micrometers. While silicon wafers have been the standardized substrate, the same fabrication can be conducted on PaC-coated substrates. Such ultrathin flexible devices made possible the post-fabrication transfer of the OECT onto soft biological surfaces granting to record electrophysiological signals.[57,58]

Like metals, metal nanoparticles, and dielectric materials, OMIECs can be processed using mass production-oriented techniques such as inkjet printing,[59,60] spray printing, or roll-to-roll fabrication.[61] Although the resolution enabled by printing techniques cannot be sub micrometers; they present an appealing alternative to the time- and cost-demanding cleanroom fabrication for applications that do not require high speeds and where cost-effectiveness is more important than performance. All OMIEC-based devices (active area and contacts) can be inkjet printed in a single step on substrates incompatible with photolithography, such as paper or thermoplastics.[62,63] Screen-printing technology is particularly suitable for large-scale production of OECT arrays, enabling, for example, the fabrication of 760 OECTs on one A4-sized sheet of polyethylene terephthalate (PET) with a yield of 99.7%.[64] Spray-deposition of OECTs offers excellent control of the OMIEC thickness through the compressed air pressure and the number of coating cycles.[65] Moreover, this technique is hardly limited by the desired type of substrate; examples include ethyl-cellulose, natural leaf, adhesive bandage, and an elastomer.[66] The rheology of inks can be leveraged for volumetric printing where every component (conductor, semiconductor, insulator, and electrolyte) can be developed as a viscous ink to realize a fully 3D printed OECT. Stereolithography has appeared recently as a technique to fabricate 3D-OECT; after optimizing a mixture of OMIEC and photocurable resin, a

1004 | Chem. Soc. Rev., 2023, 52, 1001–1023

This journal is © The Royal Society of Chemistry 2023

laser head locally exposes and crosslinks the desired volumetric design.[67] 3D printing and stereolithography are mask-free techniques suitable for rapid prototyping as only 3D models are required. Although the resolution of both methods remained above 100 μm, about 2 orders of magnitude above the standard photolithography, fabricating out-of-plane OECTs paves the way for more complex and richer architectures.

Besides printing, the polymer films can be processed at room temperature in ambient conditions using solution-based methods ranging from spin-cast, drop-cast, and doctor blade to electrodeposition,[68] electrospinning,[69,70] and freeze-drying.[71] The compatibility with a wide range of processing means enables the generation of films with various form factors such as scaffolds[71,72] or fibers[69] that can be integrated into an OECT architecture, realizing 3D or 1D channel, respectively (Fig. 1A). OMIEC fiber-based OECTs can be obtained by coating commercial fibers (often cotton or Nylon) with an OMIEC solution[73] or via electrospinning of the semiconducting fiber directly.[74] Fibers can be brought together, i.e., woven, to form a flexible fabric OECT inside a diaper, which can be further bio-functionalized to detect glucose levels in the sweat.[75] 3D channels can be generated using freeze drying, during which the solvent of the OMIEC formulation is sublimated (solid-to-gas transition), and the pores left by the sublimed solvent generate a 3D structure. Only a few solvent types can undergo sublimation (thermodynamical triple point required); therefore, the technique has been limited so far to water-based formulations. When such a polymer-based scaffold is fabricated inside a fluidic tube, and electrically connected to source–drain and gate contacts, it is possible to generate a 3D OECT. Fluidic integration supports a 3D cell culture growing inside the scaffold under constant fluid flow, while the channel current becomes a measure of cell adhesion and growth.[71]

2.2. Operation

The OECT operation starts with applying a voltage at the gate electrode (V_G), which causes a movement of ions in the electrolyte as well as in the channel (Fig. 2A). The channel current (I_D) is monitored by applying a source–drain voltage (V_D). I_D is proportional to the number of mobile charge carriers (holes or electrons for a p-type or n-type semiconductor, respectively) and their speed. In standard operation, the gate and drain voltages are applied with respect to the source electrode, which is grounded. The V_G triggers ion injection into the channel and can as well cause the ejection of counterions from the channel if they are mobile enough, which might enhance electrochemical doping.[76] Some conjugated polymers, known as polyelectrolytes, contain mobile charges that may be ejected toward the gate electrode as the bias is applied for the first time.[77] In other
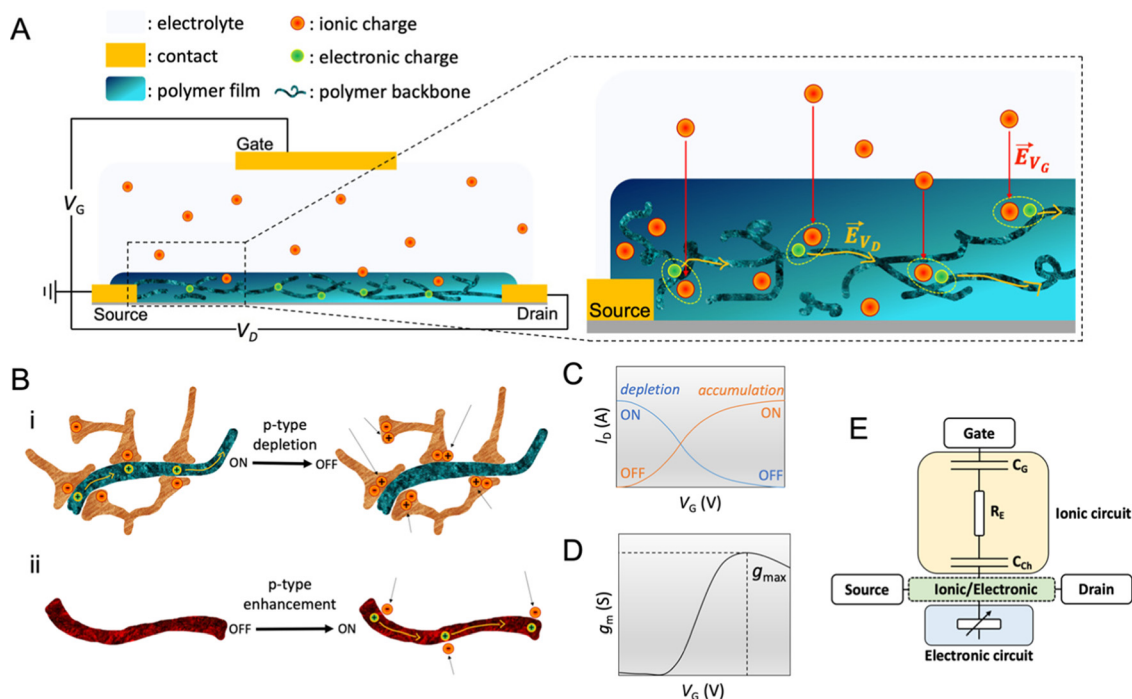

Fig. 2 OECT operation (A) schematic representation of an OECT during operation. The electric field arising from the gate electrode ($\vec{E}_{V_G}$) pushes ionic charges inside the OMIEC channel. These ionic charges stabilize electronic carriers in the channel. Electronic charges can move across the channel due to voltage applied at the drain ($\vec{E}_{V_D}$), generating a source–drain current. (B) Schematic displaying two p-type OECT modes of operation (i) depletion mode device where cations penetrating the channel deplete the holes by compensating with anionic species. (ii) Enhancement mode device where penetrating anions stabilize holes. (C) Transfer curve of an OECT working in depletion mode (blue, ON to OFF) or enhancement mode (orange, OFF to ON). Adapted with permission from ref. 41. Copyright 2021, American Chemical Society; (D) transconductance vs. V_G plot, i.e., the first derivative of the transfer curve. The transconductance of OECT typically denotes a maximum, g_{max}, reported as one of the steady-state figures of merit of OECT; (E) electronic circuit used to model OECT behavior.[88] The resistor is the electrolyte resistance (R_E), while the capacitors represent the capacitance of the gate electrode (C_G) and the capacitance of the channel (C_{Ch}). Adapted with permission from ref. 41. Copyright 2021, American Chemical Society.

This journal is © The Royal Society of Chemistry 2023

Chem. Soc. Rev., 2023, 52, 1001–1023 | 1005

cases, the film may contain ions that have diffused from the electrolyte. The electrolyte gating in OECTs allows for low-bias operation, typically below 1 V.

OECTs display two operation modes: depletion and accumulation (enhancement). The distinction between these two modes lies in the intrinsic doping state of the channel material. If the channel is made of a conducting (doped) polymer, the device operates in depletion mode (ON to OFF). In contrast, an undoped polymer with negligible electronic conductivity will work in enhancement mode (OFF to ON). An example of a depletion mode OECT comprises a poly(3,4-ethylenedioxythiophene):poly(styrene sulfonate) (PEDOT:PSS) channel (Fig. 2B-i). The net negative charges of the PSS compensate for the positive charge carriers (holes) of PEDOT, rendering the film conducting in its neutral state, with reported electrical conductivities as high as 4000 S cm^{-1} (with sulfuric acid post-treatment).[31] A positive voltage at the gate with respect to the source electrode injects electrolyte cations that pair with the PSS anions while holes are extracted at the drain electrode. The "dedoping" of the PEDOT:PSS film during the OECT operation (V_D magnitude increasing to a more positive value) causes the I_D to decrease (Fig. 2C). This process is reversible: when V_G is reversed (or stopped), cations leave the channel, and PSS once more forms ionic bonds with PEDOT, oxidizing it back to its conducting state.

It is also possible to operate PEDOT:PSS in enhancement mode OECT if the film contains aliphatic amines as de-dopants, for instance, polyethyleneimine (PEI),[78] diethylenetriamine (DETA),[79] and 1,8-diazabicyclo[5.4.0]undec-7-ene (DBU).[80] In this case, the material's conductivity is low, but there are still states that can be filled with electrochemically injected charges. In a p-type enhancement mode OECT, a negative V_G pushes anions inside the film, stabilizing holes injected along the backbone (Fig. 2B-ii). The electrostatic coupling between electronic and ionic charges increases the conductivity of the channel, switching the device from an OFF to an ON state (Fig. 2C). Other enhancement mode OECTs use conjugated polymers that contain polar, hydrophilic units, such as conjugated polyelectrolytes with charged units on side chains or polymers with ethylene glycol (EG) side chains. These polymers can be hole (p-type) or electron (n-type) transporters. One example of n-type OECT channel material is poly(benzimidazobenzophenanthroline) (BBL). The planarity and rigidity of the BBL backbone promote electron delocalization and facilitate intramolecular charge transfer. The high performance of enhancement mode BBL OECTs have been leveraged to build complementary circuits[81–83] and an ion sensor,[84] as well as neuromorphic devices.[85] Furthermore, BBL represents the first demonstration of an n-type depletion mode OECT, where BBL was chemically reduced with PEI in printable ethanol-based ink.[82] After thermal activation under an inert atmosphere, BBL:PEI films displayed an electrical conductivity as high as 8 S cm^{-1} and excellent thermal, ambient, and solvent stability. Recent work also showed the combination of p and n-type polymers in the form of a bulk heterojunction, where a p-type 6H-pyrrolo[3,2-b:4,5-b′]bis[1,4]benzothiazine ladder (PBBTL)

polymer was blended with BLL, producing an ambipolar OECT.[86] By optimizing the mass ratios of the individual polymers, the authors tuned the transport properties of each component of the bulk heterojunction, achieving a bi-continuous network of homogeneously distributed junctions between the PBBTL and BBL interfaces. Such combinations allow for extending the operation regime of OECTs. Furthermore, polymers displaying different redox states over a wide electrochemical window, such as polyaniline, can be leveraged to build single-component complementary circuits.[87]

The transconductance $\left(g_m = \dfrac{\partial I_D}{\partial V_G} \right)$ is usually considered the most important figure of merit of OECTs as it quantifies the amplification factor. It is often reported as the maximum transconductance (g_{max}) when comparing the performance of different OECTs of the same geometry (Fig. 2D). Bernards and Malliaras were the first to develop a mathematical prediction of OECT g_m by considering the conjugated polymer channel as the conjunction of an electronic circuit and an ionic one (Fig. 2E).[88] The electronic circuit is represented by a variable resistor corresponding to the conductivity of the channel that varies in function of the gating. It involves the electronic charges in the channel that drift under the application of a source–drain voltage ($\vec{E}_{V_D}$ in Fig. 2A). The ionic circuit is composed of capacitors in series with a resistor. The ionic circuit describes the flow of ions toward the semiconductor bulk and is represented by a resistor (flow of ions) in parallel with a capacitor (storage of ions). The ions drift under the application of V_G ($\vec{E}_{V_G}$ in Fig. 2A). Bernard's model considers a purely capacitive process for the film and assumes a voltage-independent electronic mobility.[89,90] The model provides a good approximation of the steady-state performance of OECTs at saturation conditions and allows for the prediction of the g_m as expressed in eqn (1):[91]

$$g_m = \frac{Wd}{L} \times \mu_{OECT} \times C^\star \times |(V_T - V_G)| \qquad (1)$$

where W and L are the width and length of the channel, respectively, d is the film thickness, μ_{OECT} is the electronic charge carrier mobility, $C^\star$ is the volumetric capacitance, V_G is the gate voltage, and V_T is the threshold voltage. According to this equation, g_m is device geometry dependent, thus, it is best to normalize it with the device dimensions when comparing the steady-state performance of different devices (see eqn (3) below). The dependence of g_m on the device geometry is not well understood and is poorly captured by current capacitive device models. Paudel et al. attempted to describe this scaling law with a 2D device model to account for the drift and diffusion of ions within the channel.[92] The model considers the equilibrium of the OECT by treating both ion and hole currents consistently in two dimensions (parallel and perpendicular to the channel). It was found that the ion concentration in the channel was not proportional to the channel potential and instead accumulated at the drain contact, influencing the device operation regime. The authors explained the bell-shaped g_m, characterized by the maximum transconductance $g_{m,max}$,

1006 | *Chem. Soc. Rev.*, 2023, **52**, 1001–1023

This journal is © The Royal Society of Chemistry 2023

as the transition point between the accumulation and depletion regimes of the PEDOT:PSS OECT, and was found to be scaling linearly for low $\frac{Wd}{L}$ channel dimensional ratios before saturating for high ratios. They showed that the V_G corresponding to $g_{m,max}$ depended on V_D and the channel thickness and length. Moreover, the authors adjusted their model to include the influence of contact resistance, which was shown to be the origin of the $g_{m,max}$ saturation at high channel ratios, and more pronounced at low V_D. Overall, this model allows to optimize the g_m by adjusting the channel ratio and biasing conditions to operate the OECT at voltages that lead to highest g_m.

Another metric in the equation above is the product of μC^*, which is commonly used to benchmark materials' mixed conduction performance. Here, C^* reflects the extent of ion penetration, transport, and storage ability of the OMIEC film. The ion uptake in the bulk of the channel yields high capacitance, hence, excellent signal amplification. The μ accounts for the transport of the electronic charges across the channel. Both of these parameters are typically V_G-dependent. Furthermore, the size, charge, and polarity of ions are parameters that influence their penetration and mobility inside the polymer film, thus influencing the μC^*.[93–95] Cendra et al. studied the effect of various compensating anions on the performance of a p-type enhancement mode OECT.[94] They found that larger and less hydrated anions lead to OECTs with higher g_m. Flagg et al. demonstrated anion-dependent doping and charge transport of p-type enhancement mode OECTs, where higher drain currents and lower threshold voltage were observed with a molecular anion (PF_6^-) rather than a smaller atomic anion (Cl^-).[30,93] Finally, OECT performance is affected by the nature and the geometry of the gate electrode as it dictates the amplitude of the gate voltage drop across the channel.[96,97] In the case of a non-polarizable gate electrode such as Ag/AgCl, most of the applied gate voltage drops at the channel/electrolyte interface. For polarizable gates, an electrochemical double-layer capacitance forms at the electrolyte interface, which, for maximum channel current modulation, should be much higher than the capacitance of the channel. It is thus required to have a large area gate when using polarizable gate electrode materials to operate the device efficiently.

Although the interactions of ionic and electronic charges in the bulk of the channel endows OECTs with high g_m, volumetric charging leads to a slow operation.[1] The response time of the OECT, i.e., the switching speed, is governed by how fast each type of charge travels inside the channel. For PEDOT:PSS, it is often the ionic charge transport that is identified as the speed-limiting process, as hole transport is relatively faster, and the response time can then be estimated from the RC time constant of the ionic circuit.[88] The response time of the OECT thus depends on the capacitance of the material, which increases with film thickness.[91] The film's thickness can thus be optimized to better match the requirements of the end application with a trade-off between the gain and the bandwidth. The following sections will detail these performance metrics.

2.3. Characterization of an OECT

2.3.1. Steady-state characteristics. The OECT steady-state performance is evaluated by recording the output and transfer characteristics. The output curves show the evolution of I_D, probed as a function of V_D, under various V_G (Fig. 3A). At a given V_G, I_D increases linearly with V_D, up to a V_D value, after which it becomes constant, i.e., reaches saturation. The pinch-off voltage (V_P) marks this transition and corresponds to the voltage at which the transistor switches from a linear to a saturation regime (Fig. 3A).[98] For some devices, the channel current may show a slight decrease at high V_D, deviating from an ideal saturation behavior.[6,93,99] Flagg et al. discussed that this decrease might be due to a spatially non-uniform charge carrier mobility throughout the film bulk, carrier repulsion occurring at high carrier densities, or because the charges reach a saturation velocity.[93] If the shape of the curves cannot be reproduced in successive cycles, the channel material likely has some irreversible redox activity or may have (partially) delaminated from the substrate. Deviation from the ideal saturation regime may also be seen if the scan rates are fast. We emphasize the importance of the sweep rate used to collect the steady-state characteristics. Changing the biases too fast will prevent the device from reaching a steady-state operation, which will be observed as hysteresis, i.e., a mismatch between the forward and backward scan in the output (or transfer) curves (Fig. 3C). The optimal sweep rate is achieved when the channel current is no longer dependent on the sweep rate. This optimal rate can be estimated by recording the transient characteristics of the device, discussed in the upcoming section.

The transfer curve is obtained by recording the channel current as the V_G is swept and the drain electrode is polarized at a constant potential with respect to the source (Fig. 3B). The V_D is typically chosen to be in the saturation regime. We obtain key parameters from transfer curves such as the V_T, ON/OFF ratio, and g_m. The V_T can be determined by plotting the square root of the I_D as a function of V_G (Fig. 3B). The linear portion of the slope with the maximum magnitude is extrapolated, and the intersection with the x-axis gives the V_T.[100] The accuracy of this method is, however, questionable given the voltage dependence of μ,[101] the presence of parasitic resistance, and the limited speed of charges at low ionic dopant concentrations.[30]

V_T is generally regarded as the voltage that fills trap states in the semiconductor for the conduction to occur in field effect devices.[102,103] In OECTs, it is mainly governed by the energetics of the channel material (ionization potential or electron affinity) and the film's readiness for ion penetration. V_T is often correlated with the electrochemical potential that corresponds to the UV-VIS polaron absorption onset. It also often matches the electrochemical onset potential (reduction or oxidation onset) identified in cyclic voltammetry curves.[94] Controlling V_T has been of particular interest for OECT-based sensors[104] and logic circuits as it dictates the noise margin and the circuit power consumption.[105] V_T has been shown to vary by the gate electrode type and electrochemical potential,[37,105,106] the side-chains of the polymer which affect ion penetration,[107] the type

This journal is © The Royal Society of Chemistry 2023
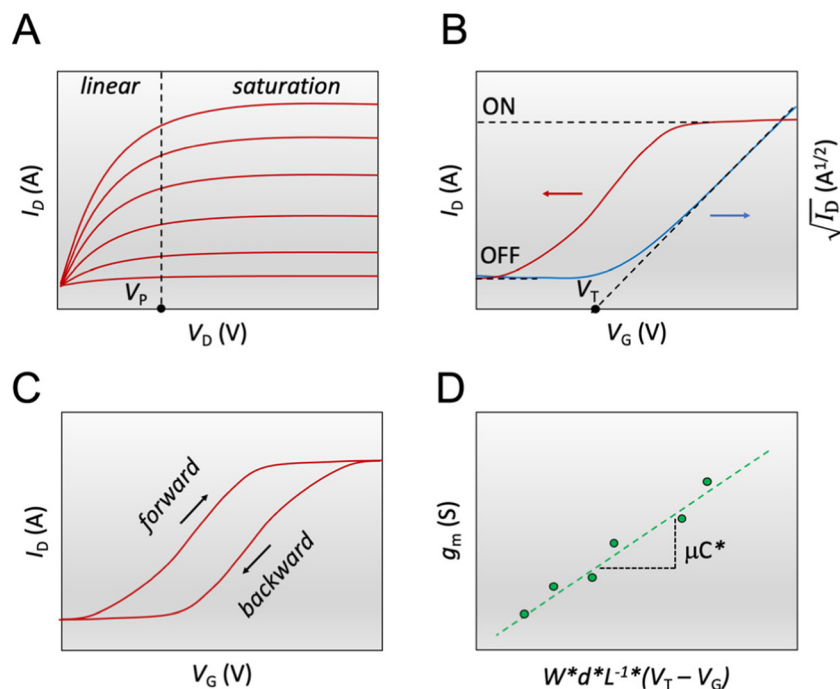
Chem. Soc. Rev., 2023, 52, 1001–1023 | 1007

Fig. 3 The steady-state figures of merit of an OECT. (A) Output characteristics show the I_D evolution as a function of V_D. Each line represents the device current at a constant V_G. The pinch-off voltage V_P is marked. (B) The transfer curve (red) shows the evolution of I_D as a function of V_G. The ON/OFF ratio is calculated from the ratio of the maximum I_D at saturation (ON) and the current at saturation in the OFF state (OFF). $\sqrt{I_D}$ as a function of V_G (blue) with V_T obtained from the x-axis intercept; (C) transfer curve hysteresis; (D) the μC^* product as an OECT figure of merit. The g_m of each OECT measured at the saturation regime is plotted as a function of its channel geometry and biasing conditions. Each point corresponds to one OECT measurement, and all the measurements give a linear relationship according to eqn (2), where the slope is the μC^* product.

and concentration of ions in the electrolyte,[93,94,104] and device architecture such as dual-liquid gate,[108,109] microfluidic channels[13] or channel aspect ratio.[110]

The ON/OFF ratio is defined as the ratio of the maximum channel current when the OECT is turned on (for an enhancement-mode transistor) and the current at OFF state (at $V_G = 0$ V if the material is undoped at this voltage) (Fig. 3B). Transistors with large and stable ON/OFF ratios are preferred for logic circuits and neuromorphic applications since high and static ON currents allow for effective signal output. Low OFF currents consume less power and cause less background noise for sensors.[64] High ON/OFF ratios are essential for biosensors' response as it improves the signal-to-noise (SNR) ratio of the device. Thus lower limits of detection can be achieved.[13,111] To this end, enhancement mode devices are preferred as they generally present higher ON/OFF ratios than depletion mode transistors (due to incomplete dedoping of the channel), and thus offer a more extensive range of current modulation.

The first derivative of the transfer characteristics corresponds to the V_G-dependent g_m at a chosen V_D in the saturation regime (Fig. 2D). Eqn (1) showed that g_m in the saturation region depends on the channel dimensions, the channel material properties (μ_{OECT} and C^*), V_T, and V_G (Fig. 3D). For the same material and device geometry, any condition that impacts V_T will naturally change the g_m. The reported g_m values are typically normalized by the width of the channel transistor,

film thickness, or sometimes the V_D, indicating the lack of a standard.[2,77,112] As g_m is one of the main performance metrics, it is crucial to have a standardized way of reporting it for a fair comparison between different devices. The following equation normalizes the g_m with the device geometry:

$$g_m(\mathrm{NR}) = \frac{g_m \times L}{W \times d} \tag{2}$$

When determining $g_m(\mathrm{NR})$, we stress the importance of accurate thickness measurements. While it is common to normalize the g_m by the thickness measured from a film cast using the same conditions but on a usually much bigger electrode (typically made of gold), these values do not necessarily correspond to the film thickness in the microscale channel, especially when it is fabricated using the photolithographic process described above. The thickness mismatch is severe where the channel opening leads to a significant difference in the polymer's wetting, and thus coating, compared to a large electrode surface. Even the thickness of the film cast on a metal electrode microfabricated on the same substrate and located in the vicinity of the channel may differ from that in the channel. For accurate channel thickness measurements, atomic force microscopy measurements are recommended, where the film is scratched down to the substrate, typically using a hard tip in contact mode. This method is, however, time-consuming and destructive to the channel. An alternative is fabricating a separate device without the metal contacts through the same

1008 | *Chem. Soc. Rev.*, 2023, **52**, 1001–1023

This journal is © The Royal Society of Chemistry 2023

protocol used for patterning and measuring the film thickness with a profilometer. This way, the channel wetting, and coating properties can be routinely replicated on a separate substrate and used only for film thickness estimations. As for the length and width, they should be measured each time after fabrication to eliminate batch-to-batch differences. We define the length of the channel as the distance between the source and drain electrodes, and thus do not consider the overlap between the channel and the contact electrodes.

2.3.2. Transient characteristics. Since OECTs operation involves ion penetration and transport inside the channel, the time it takes for the device to switch ON or OFF is longer than field effect transistors (FETs). OECTs typically operate in the 10–100 kHz range, while FETs can function up to the MHz range. The response time is limited by either the electronic or the ionic circuit, depending on the speed of the corresponding charge carriers.[88] At constant biasing conditions, the time dependence of I_D change can be estimated by considering how fast the channel takes up ionic charges. Assuming a uniform doping (de-doping) process in the channel without saturation effects, Bernard's model predicts that the I_D response to a square V_G pulse has an exponential time dependence (Fig. 4A):[88]

$$I_D(t) = I_{SS}(V_G) + \Delta I_{SS}\left[1 - f\frac{\tau_e}{\tau_{On}}\right]e^{\left(-\frac{t}{\tau_{On}}\right)} \quad (3)$$

where $I_{SS}(V_G)$ is the steady-state channel current at the applied V_G, ΔI_{SS} is the difference between the initial and final steady-state currents (i.e., I_{ON}–I_{OFF}), f is a weighting factor corresponding to the I_G contribution to I_D, τ_e is the transit time of electronic charges in the channel, and τ_{On} corresponds to the

RC time constant: $\tau_{On} = R_S \cdot C_{Ch}$, with R_S being the electrolyte resistance and C_{Ch} the channel capacitance. C_{Ch} scales linearly with the channel volume, while R_S is proportional to the $1/\sqrt{WL}$.[113] The relaxation of the I_D over time is fitted with a mono-decay exponential function, where the characteristic time corresponds to the time response of the OECT (τ_{On}).

According to eqn (3), when the electronic transport is faster than the ionic charging, I_D relaxes monotonically to its steady-state value (Fig. 4A-i). When the electronic transport is instead the limiting factor, I_D displays a spike beyond the final steady-state current before relaxing exponentially towards the final current, demonstrating a "spike and recovery" behavior (Fig. 4A-ii). The monotonous relaxation and "spike-and-recovery" behavior of channel current have been observed for various OECTs.[91,98,114–116] The OECT transient characteristic is thus generally measured from the I_D response to a V_G pulse, under a constant V_D (chosen in the saturation regime). The V_G pulse amplitude and period are adjusted depending on the material and channel geometry. For example, a large channel geometry typically leads to slower devices. Hence the pulse length should be correspondingly extended. Using a long gate pulse would be appropriate to obtain a current response with high resolution for a good quality fit.

Another method to estimate τ_{On} is through the impedance matching method, detailed below for the determination of μ_{OECT}. Here, τ_{On} can be calculated from $\tau_{On} = R_S \cdot C_{Ch}$ after modeling the impedance spectra with an equivalent circuit model or through the cutoff frequency (f_c), which describes the frequency upper boundary that OECTs can achieve for signal acquisition and amplification (Fig. 4B), based on eqn (4):[117]

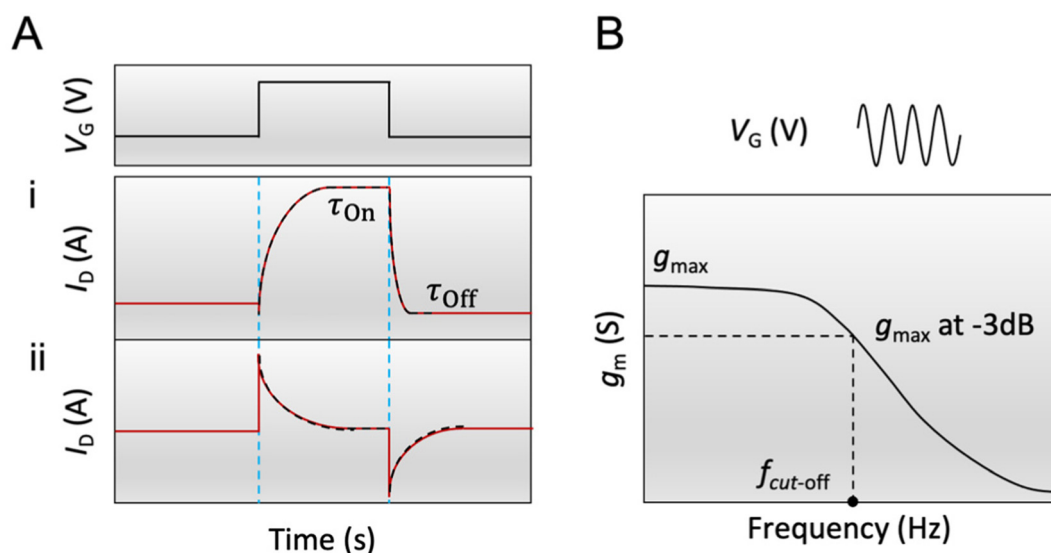$$\tau_{On} = \frac{1}{2\pi f_c} \quad (4)$$

Fig. 4 The transient characteristics of an OECT (A) I_D in response to a square V_G pulse is measured while V_D is maintained constant. Two main types of behaviors are observed: a monotonic relaxation of I_D towards the steady-state value (i) or a "spike and recovery" behavior (ii). The fit is an exponential decay function (black dotted lines), from which the characteristic time is extracted; (B) g_m is measured in response to a sinusoidal V_G pulse while V_D is maintained constant. The frequency corresponding to the value of g_{max} at −3 dB (around $0.707g_{max}$) represents the cut-off frequency of the device that can be used to estimate τ_{On}.

This journal is © The Royal Society of Chemistry 2023

Chem. Soc. Rev., 2023, **52**, 1001–1023 | **1009**

where f_c corresponds to the frequency of the g_m at -3 dB (ca. $0.707g_{max}$). Although this method has been rarely reported in evaluating τ_{On} compared to transient measurements in response to a DC gate pulse, response times calculated through both techniques have been shown to be relatively similar.[91,118] The estimation of τ_{On} through impedance fitting also allows for simultaneous determination of the capacitance (see the section below).

Some strategies have been implemented to shorten the OECT response time to meet the needs of the end application. In the first method, the film is made thinner, or the dimensions shrink (mostly by reducing W) as $\tau_i \propto d/\sqrt{WL}$.[90] Given the relationship between channel geometry and g_m (eqn (1)), L should be as small as possible to maximize g_m, while W and d should be chosen considering the application. For instance, when using OECTs to measure slow signals of low amplitude, W and d should be increased, while a thinner and narrower channel will be more beneficial for fast signals. A second method is to optimize the biasing conditions. Friedlein et al. demonstrated that by operating OECTs at $V_D = V_{STEP}$, OECTs could respond more than 30 times faster than the speed of their ionic charging circuit, where:[98]

$$V_{STEP} = -\frac{L^2}{2\mu_{OECT}R_S C_{Ch}} \quad (5)$$

V_{STEP} marks the boundary between a monotonic and spike-and-recovery response, with $0.5I_{G,max} = \Delta I_{SS}$ at V_{STEP}. However, V_{STEP} might not be large enough to operate certain electronics (like diodes), or limit the OECT gain and ON currents. Donahue et al. introduced an alternative architecture, who vertically built the channel, resulting in vertical OECT (vOECT).[54,119] vOECTs represent an attractive device to decrease the device footprint while displaying superior electronic properties. The authors demonstrated higher g_m and faster switching speed on PEDOT-based vOECTs (Fig. 1B-iv), where the length of the channel (corresponding to the insulating layer between the drain and source contacts) can be decreased to dimensions outside photolithography limits (down to 450 nm from typically 5 μm achieved by photolithography).[54,119] In another effort, Spyropoulos et al. developed the ion-gated organic electrochemical transistor (IGT), addressing the ion transport limited device speed issue.[120] The authors encapsulated mobile ions in the channel using D-sorbitol acting as an ion reservoir and conductivity enhancer, significantly reducing the device's response time down to 31.7 μs. Finally, the molecular structure of polymer backbones, especially the side-chain design and film processing technique, have been shown to influence τ_{On}.[121] Chen et al. investigated the impact of varying the side-chain structure on ethylene glycol (EG)-substituted polythiophenes.[122] The authors found a faster doping speed as the side chains were made to be more hydrophilic, suggesting that the increased hydrophilicity facilitated ion transport within the film. In addition, the authors demonstrated that the presence of a polar functional group (oxygen) further away from the backbone is beneficial for ion movement and, thus for the device switching speed.

The authors demonstrated that the material dedoping kinetics (i.e., device turn OFF times) were less affected by the side chains. Savva et al. showed that side-chain hydrophilicity was a critical design parameter for high-performance OECTs, where too much water uptake decreased g_m and increased τ_{On}.[123]

While Bernard's model marks the first attempt to predict OECTs' transient response, the simplifications introduced in the model limit its accuracy, which was addressed in more recent models. For example, Friedlein et al. considered an exponential distribution of the density of states. They accounted for the influence of the charge carrier density on μ_{OECT} to address the constant charge carrier mobility assumed in Bernard's model.[124] The authors proposed that their non-uniform mobility model will be helpful in better understanding the transient behavior of OECTs. Other models have improved Bernard's model and given a physical interpretation to the factor f (see eqn (3)). Gentile et al. proposed a hybrid model combining Bernard's and the equivalent circuit models, associating f with the penetration depth of ions in the film bulk, where the output characteristics of the device depend explicitly on the size and charge of the ions species.[125] Fitting the model to channel current response to triangular gate voltage pulses could describe the transient response of OECTs and be used to calculate ion diffusion coefficients in solution, where the lag between the doping and dedoping peak current at different frequencies was characteristic of a specific system diffusivity. They used this method to discriminate electrolyte characteristics such as the cation and anion type and their concentration. Based on equivalent circuits, Faria et al. introduced a model that could accurately predict OECT transient behavior and provide an experimental method to determine the factor f.[116] By fitting the gate and channel current response to a V_G pulse, the model yields impedance circuit values such as the impedance (capacitance and resistance) of the polymer in the channel, the electrolyte resistance, and, ultimately, the factor f. I_G that flows into the channel is split between the source and drain electrodes. The authors interpreted factor f as the fraction of this current measured at the drain electrode and demonstrated that it was gate and drain voltage-dependent. They further speculated that f also depends on the channel geometry and gate-channel distance. Faria model was extended to describe the behavior of cell membrane integrated OECTs and to effectively extract the corresponding membrane impedance characteristics, parameters that define their health status. For an in-depth analysis of the current OECT models and their limitations, along with the physical phenomena considered, we would like to refer the reader to recent literature reviews and ref. 22, 90, 103, 126 and 127.

3. Characterization of mixed transport properties of OECT channel

3.1. Volumetric capacitance (C^*)

The capacitance of a material is often determined from the electrochemical impedance spectrum (see Fig. 5A for an
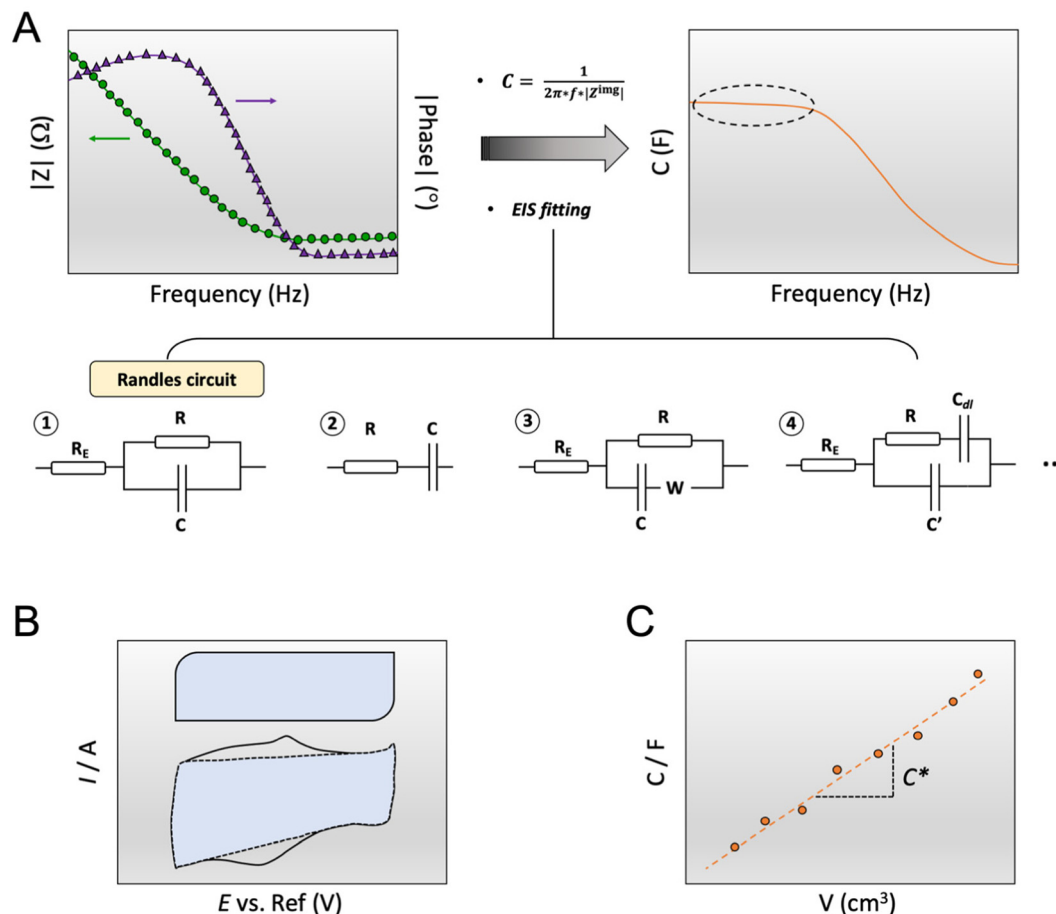
1010 | Chem. Soc. Rev., 2023, 52, 1001–1023

This journal is © The Royal Society of Chemistry 2023

Fig. 5 Determination of C^*. (A) C extraction from EIS data (left plot: dots and triangle represent the impedance modulus $|Z|$ and the impedance phase, respectively) either by applying eqn (6) (right plot, the marked area shows the plateau at low-frequency region) or by fitting the data with an equivalent circuit modeling. The most common equivalent circuit models are shown at the bottom; (B) C extraction from the integration of a cyclic voltammogram curve, represented by the blue area, according to eqn (8). The top box-like curve represents an ideal capacitive material, while the bottom curve corresponds to an OMIEC that presents redox reactions; (C) C vs. volume curve. The slope yields C^*.

exemplary spectrum) recorded using electrochemical impedance spectroscopy (EIS). The EIS setup involves a three-electrode system with the OMIEC film addressed as a working electrode (WE), a reference electrode (RE), and a counter electrode (CE), all immersed in the electrolyte. The CE should have a much larger C than the WE to ensure that the kinetics of the reactions occurring at the counter do not inhibit those occurring at the WE.[128] The spectrum is acquired by applying a small AC modulation (typically 10–50 mV) with varying frequencies (typically 10^6–10^{-1} Hz) on a DC offset. The voltages are applied to the WE with respect to the RE. The spectrum will naturally change as a function of the offset voltage and for undoped films, the spectrum should be acquired at a potential that maximizes the C of the OMIEC film. For intrinsically doped polymers such as PEDOT:PSS, the voltage is set at the open circuit potential. Once the data are acquired, the C can be extracted in two ways. The first approach relies on eqn (6):[129]

$$C = \frac{1}{2\pi \times f \times |Z^{\mathrm{img}}|} \qquad (6)$$

where Z^{img} (Ω) is the imaginary part of the impedance and f is the frequency (Hz). This method can be used if the impedance phase angle, corresponding to the time shift between the voltage applied and the current detected, is associated with a capacitive-like behavior. For a perfect resistor, the phase angle is $0°$, while for an ideal capacitor the phase angle will be $90°$. The output will be a plot of C as a function of f, ideally displaying a plateau at low f range (Fig. 5A, right). The C value should be reported at the low-f region of the spectrum (0.1 or 1 Hz), where the AC modulation is slow enough to give enough time for the ions to populate the film.

The C extracted this way includes all the possible capacitive contributions of the system. In the case where a material deviates from an ideal capacitor behavior, evidenced by an impedance phase angle much lower than $90°$ at low frequencies, the contribution of a double layer capacitance, C_{dl}, becomes significant. Such materials are those with low ionic mobility or high ion injection barrier, thus the impedance phase spectrum is an important aspect to analyze to determine whether a material would work in an OECT device. C_{dl} can be

This journal is © The Royal Society of Chemistry 2023

Chem. Soc. Rev., 2023, **52**, 1001–1023 | 1011

calculated as the slope of the difference in anodic (j_A) and cathodic (j_C) current density (A/unit area), measured in the non-faradaic region (at a potential that does not involve any electron exchange reactions) of the cyclic voltammogram as a function of the scan rate v:[130]

$$C_{dl} = \frac{\partial(j_A - j_B)}{2\partial v} \tag{7}$$

The second way consists of using an equivalent electronic circuit model to fit the impedance data and extract the values of circuit components, including C. Simple models have been proposed to fit the impedance spectra of conjugated polymers, with the most common being the Randles circuit (Fig. 5A, circuit 1).[2] The Randles circuit is based on a resistor and a capacitor in parallel, corresponding to the polymer film resistance and capacitance, respectively, in series with a resistor that represents the resistance of the electrolyte. This fit has adequately described the charging behavior of conducting polymer films.[91,131] Such films have also been modeled using a single resistor in series with a capacitor (Fig. 5A, circuit 2), relying on the high ionic mobility in the film and the ease of ion penetration.[89,113,132–134] For some films, a Warburg element is included to account for the diffusion-limited processes (Fig. 5A, circuit 3).[129] Others have included a second capacitor corresponding to the C_{dl} (Fig. 5A, circuit 4),[135] replaced the capacitor with a constant phase element to account for the non-uniformity of the material surface,[136] or used a combination of these.[137,138] With increasing circuit complexity, the circuit elements and their relationship become less representative of the actual physical phenomena and sometimes conflicting despite the matching quality of fits to the recorded spectra. The bottom line is that there is no consensus on which universal equivalent electronic circuit model to use to fit a spectrum. However, regardless of the equivalent circuit model employed, we stress the importance of reporting the error associated with the fit for each component. For OMIECs, we expect no significant barrier for ionic/electronic charge injection, and the C values extracted from these two methods should be similar.[2,132]

Besides EIS, cyclic voltammetry also allows the C to be estimated (Fig. 5B). In the absence of faradaic reactions, the cyclic voltammogram can be integrated to provide C^*, according to eqn (8):[89]

$$C = \frac{\oint j\partial V}{2 \times v \times (V_{max} - V_{min}) \times d} \tag{8}$$

where j is the current density, V_{max} and V_{min} correspond to the voltammogram potential window, v is the scan rate, and d is the film thickness. To calculate C directly from the voltammogram integration, we assume that the polymer is operating as an ideal capacitor, meaning there is no ion barrier, no stratification, and/or accumulation of ions at the polymer/electrolyte interface. When faradaic peaks are present, the extraction of C becomes less trivial and only correct when the respective areas of these redox peaks are excluded from the integrated area.[137] Here, the selection of the scan rate is essential: a too-fast scan

rate will result in an incomplete charging/discharging of the film and, thus, an underestimation of the C. The calculation of the C from the CV has been shown to closely match the one extracted from EIS, at least for PEDOT:PSS.[89] Diffusion-controlled processes, ion speed, and any ion trapping can be possibly understood by plotting the relationship of redox peak amplitudes with the scan rate.

Lastly, to extract the C^*, one should divide the obtained C value by the corresponding film volume (Fig. 5C). For accurate estimation of C^*, the C of films with varying geometries should be measured. The extracted capacitance should scale linearly with the film geometry with the slope of the curve, yielding C^*.[2,91] The offset of the linear fit can indicate the presence of an ion injection barrier or ion accumulation at the polymer film/electrolyte interface.[91] A saturation at high film volumes may be due to an incorrect speed used to evaluate the charging currents.

3.2. Electronic charge carrier mobility (μ_{OECT})

While methods for extracting electronic mobility in (O)FET devices and their limitations are well established and documented in the literature,[139,140] the co-presence of ionic and electronic charges in the OECT channel prevents the direct translation of these techniques to extract OECT electronic charge carrier mobility in OECTs (μ_{OECT}). The determination of μ_{OECT} is based on measuring the electronic charge carrier transit time (recall, τ_e) from a time or frequency domain I_G analysis. The first approach applies an I_G pulse while the channel current is monitored at a constant V_D (Fig. 6A-i).[88] The slopes of I_D vs. time curves as a response to I_G pulses with various magnitudes is plotted as a function of I_G. The τ_e is then extracted using eqn (9):[88]

$$\frac{\partial I_D}{\partial t} = \frac{-I_G}{\tau_e} \tag{9}$$

A second method to extract τ_e, known as the impedance matching method,[118] considers the relationship between the gate and channel currents as described in eqn (9) in the frequency domain (Fig. 6A-ii). Here, a sinusoidal signal V_G is applied at the gate electrode with varying frequencies while I_D and I_G are measured simultaneously (examples at 2 Hz, 200 Hz, and 20 kHz are represented in Fig. 6A-ii). The information from the varying I_D over the V_G yields the g_m as a function of frequency, while the variations of the I_G over V_G led to the system impedance as a function of frequency. The amplitude and phase of the applied voltage and measured currents are determined from a least-squares fit to the sinusoidal signals. Finally, the conversion of I_D-deduced g_m to impedance is based on the relation between I_D and I_G, as described in Bernard's model,[88] and represented in eqn (10):

$$\Delta I_G = 2\pi \times f \times \tau_e \times \Delta I_D \tag{10}$$

Once τ_e is estimated using either of these methods, μ_{OECT} is calculated based on eqn (11):
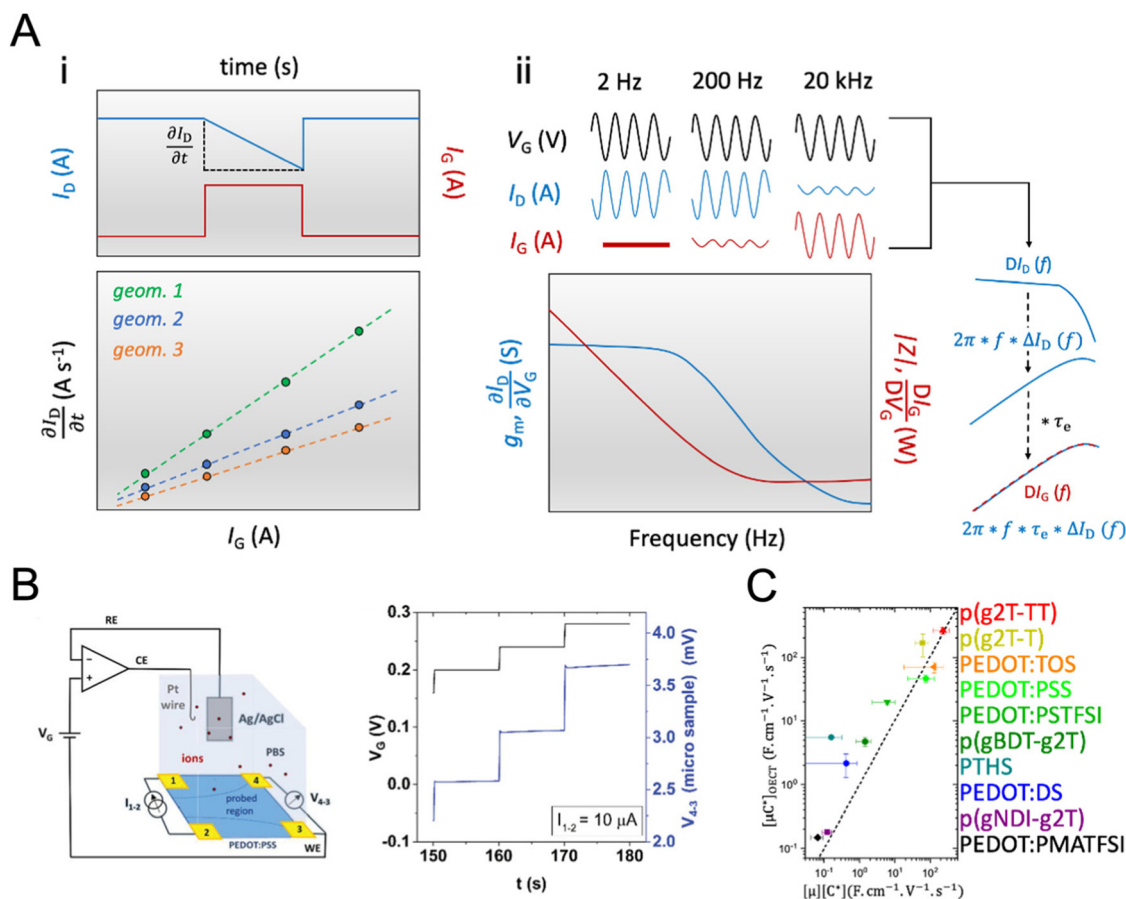
$$\mu_{OECT} = \frac{L^2}{V_D \times \tau_e} \tag{11}$$

1012 | *Chem. Soc. Rev.*, 2023, **52**, 1001–1023

This journal is © The Royal Society of Chemistry 2023

Fig. 6 Determination of μ_{OECT}. (A) The μ_{OECT} is calculated from the electronic charge carrier transit time τ_e using eqn (9). The τ_e can be determined by gate current analysis at time (i) or frequency (ii) domain. Adapted with permission from ref. 118. Copyrights 2015, AIP Publishing LLC; (B) schematic of the electrochemical van der Pauw measurement setup (left) and time response of microscopic four-contact structures during electrolyte gated van der Pauw measurements. The voltage drop on the sample between the sensing contacts 4 and 3 is measured in time while varying the applied gate voltage V_G. Adapted with permission from ref. 141. Copyright 2021 Wiley-VCH; (C) the $[\mu C^*]$ product extracted from the slope of Fig. 3C is plotted as a function of the product of $[\mu_{OECT}]$ and $[C^*]$ determined independently for various OMIECs, where the dashed line corresponds to a 1:1 agreement. In particular, p(g2T-T), p(g2T-TT), and p(gBDT-g2T) are p-type enhancement mode OECT materials based on glycolated thiophene, thiophene–thienothiophene, and benzo[1,2-b:4,5-b']dithiophene (BDT)-thiophene-based backbones, respectively. TOS, PSS, PSTFSI and PMATFSI, and DS, are molecular, polymeric, and biological anionic dopants complexed with PEDOT, namely tosylate, poly(styrene sulfonate), (trifluoromethylsulfonyl)sulfonylimide (styrene or methacrylate backbone and Li^+ as the counter ion), and dextran sulfate, respectively. These materials are suitable for p-type depletion mode operation. p(gNDI-g2T) is a glycolated naphthalene diimide-based n-type material. PTHS is a thiophene-based, undoped conjugated polyelectrolyte with sulfonate-terminated alkyl chains. Adapted from ref. 2 under the terms of the Creative Commons Attribution 4.0 International License. Copyright 2017, Nature Publishing Group.

One of the main bottlenecks to mobility measurements is the parasitic effect of contact resistance. Contact resistance originates from the energetic differences between the metal contact work function and the channel material's transport level (HOMO/LUMO). This mismatch creates an injection barrier, the Schottky barrier, that inhibits charge carrier injection/extraction. Bonafè *et al.* proposed a contact-independent version of the electrolyte-gated van der Pauw method to characterize electronic charge transport in OECTs (Fig. 6B).[141] The method uses a conventional three-electrodes setup, with RE and CE electrodes and a WE consisting of 4 symmetric gold contacts placed at the edges of a polymer film, where the contacts' dimensions are much smaller than the polymer film dimensions. A current is then injected between two contacts (high- and low-force contacts respectively, *i.e.*, contacts 1 and 2

in Fig. 6B), while the voltage drop is measured between the other two contacts (high- and low-sense contacts, *i.e.*, contacts 4 and 3 respectively, in Fig. 6B). At the same time, a V_G is applied between the reference electrode and the low-sense contact. Since the contacts that sense the voltage are non-injecting, the detrimental effects of contact resistance are bypassed. The portion of the film between contacts 4 and 3 represents an OECT channel with dimensions $\frac{L}{W} = \frac{\ln(2)}{\pi}$ in accordance with square van der Pauw structures.[142] The current injected between contacts 1 and 2, I_{1-2} can then be expressed in terms of the sheet resistance σ_S:

$$\frac{\ln(2)}{\pi} \times I_{1-2} = \sigma_S \times |V_{4-3}| \qquad (12)$$

This journal is © The Royal Society of Chemistry 2023

Chem. Soc. Rev., 2023, **52**, 1001–1023 | **1013**

From which μ_{OECT} can then be calculated as:

$$\sigma_S = \mu_{\text{OECT}} \times C \times |V_T - V_G + V_C| \qquad (13)$$

and

$$V_C = \frac{V_{4-3}}{2} \qquad (14)$$

For σ_S, the film resistance is measured between each contact is calculated as follows:

$$R_{1-2} = \frac{V_{4-3}}{I_{1-2}} \qquad (15)$$

The average film sheet resistance $\langle R \rangle$ is then used to calculate σ_S:

$$\sigma_S = \frac{\ln(2)}{\pi \times \langle R \rangle} \qquad (16)$$

while the methods relying on τ_e estimations use transient OECT data, some reports determine the saturation mobility ($\mu_{\text{OECT,sat}}$) using the steady-state characteristics. The $\mu_{\text{OECT,sat}}$ can be extracted from the slope of the square root of I_D as a function of V_G, similar to how FET mobilities are calculated:[143,144]

$$\mu_{\text{OECT,sat}} = \frac{2L}{WC^*d} \times \left(\frac{\partial \sqrt{|I_D|}}{\partial V_G}\right)^2 \text{ for } |V_G - V_T| < |V_D| \quad (17)$$

while the techniques that rely on transient methods are more suitable for materials with high mobilities, they may not be applicable for low-mobility materials ($\leq 10^{-4} \text{ cm}^2 \text{ V}^{-1} \text{ s}^{-1}$). This is because the currents recorded are noisy and do not allow for a proper fit. For such cases, μ_{OECT} can also be extracted using the g_m relationship shown in eqn (1). Once C^* is estimated from external measurements, μ_{OECT} can be determined from the μC^* product. When using this method, it is essential to determine the channel geometry accurately. For a rigorous determination, g_m and C^* should be determined for various channel geometries, such that an accurate μC^* value can be calculated, leading to less error in μ_{OECT} estimation. Overall, the μ_{OECT} values estimated using these different methods should be in the same order of magnitude. Otherwise, the quality of measurements becomes questionable. As shown in Fig. 6C, the product of independently measured values of μ_{OECT} and C^* of various materials agree mostly well with the $[\mu C^*]$ obtained from the geometry/bias-dependent g_m plot.[2] Kim et al. also demonstrated a good agreement between μ_{OECT} values of PEDOT:PSS microfibers calculated from the slope of the g_m at the saturation regime and those determined experimentally from the impedance matching method.[2,145] For relatively high mobility materials, variations and/or spreading of the values have been attributed to non-uniformities in the film formation, experimental determination of the film thickness, parasitic resistances, and edge effects.[2,90]

Finally, note that the electronic charge density varies across the film as it depends on the electrochemical potential (which has a changing profile from source to drain),[146] resulting in non-uniform, voltage-dependent charge transport properties.[124] The voltage dependence of μ_{OECT} has also been attributed to band fillings (i.e., at high doping potentials, HOMO or LUMO is filled with electronic charges, and there is a lack of empty states to allow the charge to hop onto) or contact effects. On the other hand, an ionic charge injection barrier causes the C to be voltage-dependent.[2,146,147] Thus, it is essential to keep in mind that the application of eqn (1), from which we can obtain the different steady-state figures of merit of OECT, does not take into account these considerations, and therefore voltage-dependent must be taken into account when reporting/interpreting data.

3.3. Ion mobility and ion motion

Monitoring ion transport within the channel and quantifying ion mobility is critical to improving OECT performance, particularly the switching speed and capacitance. While methods have been developed to estimate the mobility of electronic charge carriers, the ion motion in the film is not trivial to monitor, and ion mobility is more challenging to calculate due to the accompanying movement of electronic charges. Ion transport in a conjugated polymer film depends on the nature of ionic species (size, water affinity, and interactions with the counter ion), the strength of the electrical field, and on the polymer film morphology and interactions with the electrolyte (swelling). For an OECT operating in aqueous electrolytes, the channel needs to interact with hydrated ions; hence integrating polar components, such as EG units or charged groups in the polymer side chains, has been a successful strategy to enhance the ion transport ability of the films.[27,121] Increasing the segmental motion of the side chains by introducing alkyl spacers was suggested to improve ionic conductivity further.[148] Besides the nature of chemical components that make the film, the film microstructure and morphology affect ion transport.[25,149] For example, including a cross-linker such as 3-glycidoxypropyltrimethoxysilane (GOPS) in the PEDOT:PSS formulation makes the film denser (less porous), decreasing the speed of ions.[134] The addition of EG in the polymer dispersion improves the electronic charge transport by rendering PEDOT and PSS phases more homogenous and increasing the PEDOT-rich content, which, in turn, reduces the ability of ions to reach these PEDOT-rich areas.[25,149]

One method to study ion motion and extract their mobility involves a spectroelectrochemistry setup where the film's optical transmission profile or UV-VIS spectrum is monitored while it is electrochemically doped (Fig. 7A). This is possible as the electronic excitations have signatures in the optical spectrum of OMIEC films. In this experiment, the ion motion in the film is restricted to two dimensions as the film is insulated everywhere except for an opening to the electrolyte where the reference electrode is dipped.[134,149,150] Application of a potential between this electrode and the other end of the film forces ions to penetrate the film and travel towards its end. As the ions move, they change the transmission profile of the film (Fig. 7A), causing a de-doping (or doping) front to move as fast as their speed. Monitoring the evolution of this "moving front" over time allows us to estimate ionic mobility.[149,151] Stavrinidou et al. proposed a model based on these experiments
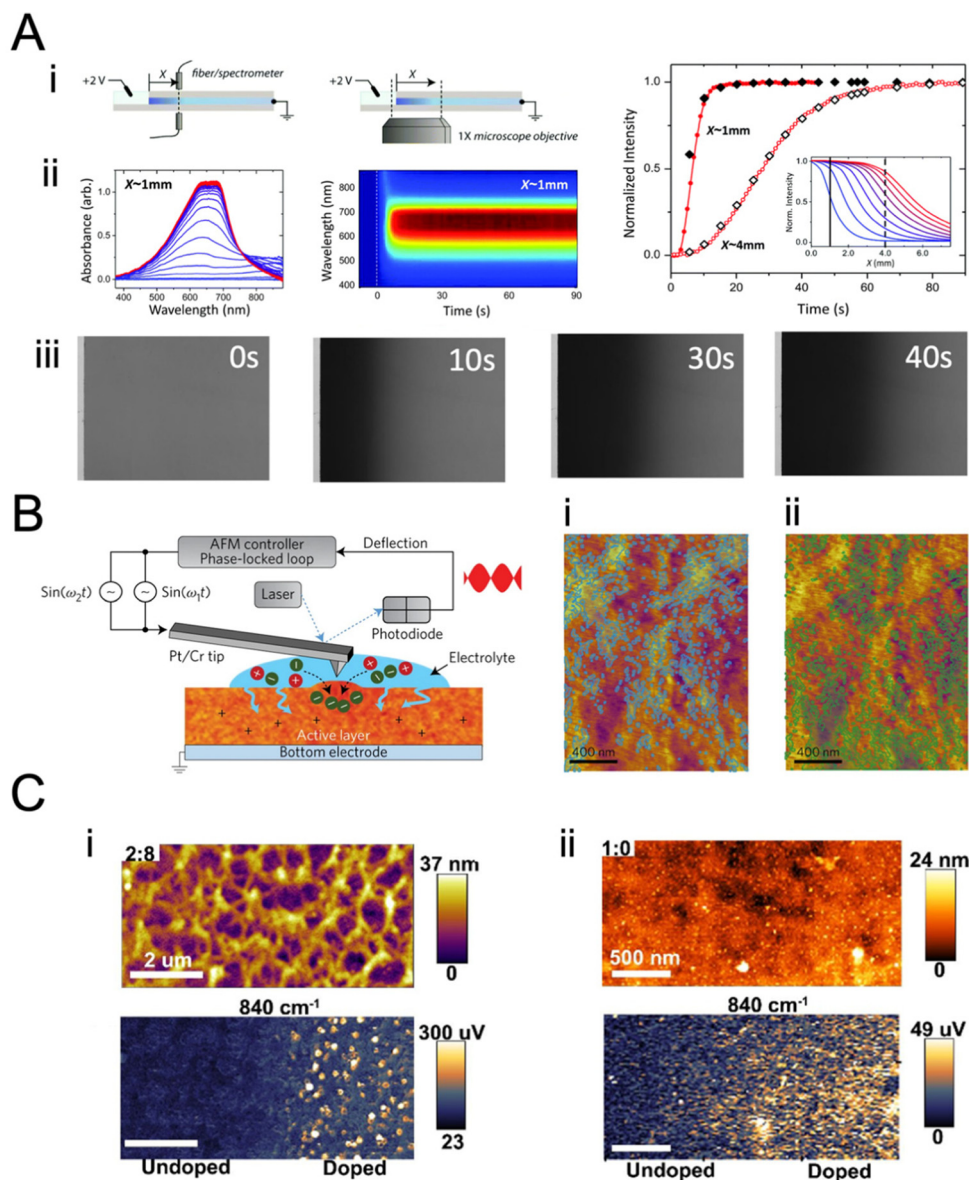
Fig. 7 Monitoring ion transport in OMIEC films. (A) (i) Moving front measurement configurations: a spectro-temporal moving front experiment using a white light source/fiber spectrometer (left) and spatio-temporal moving front experiment using a microscope objective (right) at a specified distance X from the edge of the film–electrolyte interface to track the motion of injected ions. In all cases, the time of application of bias is $t = 0$ s. (ii) The absorbance spectra and the corresponding time–wavelength color plot for $X \approx 1$ mm for a PEDOT:PSS film (0 vol% EG). The right panels show the absorbance spectra from $t = 1$ s (blue) to $t = 90$ s (red) using the same color scheme. (iii) The optical images of the moving front at $t = 0, 10, 30,$ and 40 s. (iv) Normalized absorbance intensity of the film at a distance X as the de-doping front propagates, validating the agreement between the spectro-temporal (red symbols) and spatio-temporal moving front experiment (black symbols) (X values as noted). The normalized absorbance intensity profiles of the same film obtained from microscopy studies are shown as insets (blue: $t = 5$ s, red: $t = 45$ s. Adapted with permission from ref. 149. Copyright 2016, Royal Society of Chemistry; (B) instrumentation schematic of *in situ* electrochemical strain microscopy (ESM) using dual-amplitude resonance tracking centered around the contact resonance frequency. ESM images from P3HT thin films overlaid with AM-FM pixels corresponding to the lower 21% (i) and upper 24% (ii) of AM-FM stiffness (frequency) map data, where higher frequency means higher elastic modulus. The pixels show anti-correlation between AM-FM and ESM data, with morphology ranging from more amorphous (softer) to more crystalline (stiffer) correlated with enhanced or diminished ion uptake. Adapted with permission from ref. 40. Copyright 2017, Nature Publishing Group; (C) Comparison of topographic features of two ratios of DPP-DTT:polystyrene (PS) nanowire blends upon PF_6^- doping. (i) Topography (top) and 840 cm^{-1} PiFM pixels corresponding to PF_6^- signal (bottom), for a 2:8 film. Here the nanowire film was doped at approximately half of the film. The PF_6^- ions do not appear in the topography but are very obvious in the PiFM image, indicating that the ions have penetrated the matrix. (ii) 1:0 film topography focusing on a similar doping junction (top) and PF_6^- corresponding image (bottom). Here, the topography clearly shows the PF_6^- ions, consistent with the interpretation that the ions are not penetrating the film. The PiFM image shows the same contrast everywhere, consistent with most of the anions staying closer to the surface. Both films were doped with 100 mM KPF_6 at −0.85 V. Adapted with permission from ref. 153. Copyright 2021, American Chemical Society.

This journal is © The Royal Society of Chemistry 2023

Chem. Soc. Rev., 2023, **52**, 1001–1023 | **1015**

to evaluate ion drift mobility inside conducting polymer films (*e.g.*, PEDOT:PSS).[134,151] By modeling the moving front as two resistors in series (one ionic for the dedoped part and one electronic for the doped region), the authors related the moving front length (or drift length of the injected ions), ℓ, to the total resistance of the film according to eqn (18):

$$R_{tot} = \frac{\rho_I}{S}\ell + \frac{\rho_C}{S}(L - \ell) \quad (18)$$

where ρ_I and ρ_L are the resistivities of the undoped and doped material, respectively, L is the film's total length, and S is the cross-sectional area. Assuming a complete ionic–electronic charge compensation and an ionic mobility much lower than the electronic mobility, the ion drift length, temporal dependence, and cation density can be calculated based on eqn (19):

$$\ell^2 = 2 \times \mu_P \times V_{applied} \times t \quad (19a)$$

$$j = \frac{eP\sqrt{2 \times \mu_P \times V_{applied}}}{2\sqrt{t}} \quad (19b)$$

where μ_P is the ion mobility, e is the electron charge, P is the cation density, and j is the current density. Using this model, the authors could effectively fit and predict (based on numerical simulations) the mobility of cations in PEDOT:PSS. The authors found that the estimation error increased for low applied voltage values where the assumption of complete compensation is not satisfied) and that electrolytes with low ion concentrations underestimated the ion mobility due to a voltage drop generated at the polymer–electrolyte interface.[151] The effect of GOPS inside PEDOT:PSS on ion mobility was also investigated. The additive changed the film morphology and reduced the swelling of the film with water, leading to an order-of-magnitude decrease in ionic mobility.[25,134]

Besides monitoring the transmission profiles, the same technique could monitor the evolution of the UV-VIS spectrum (Fig. 7A-ii). Doing so allows us to get more information about the preferential movement of ions to different parts of the film as the optical features at different wavelengths inform about film morphology, as they may belong to differently aggregated parts of the films. As such, ion transport-morphology relationships can be investigated. Moving front measurements, and the above analytical model, are currently the only method that allows estimating ion mobilities in OMIEC films. However, the above model has not yet been applied to intrinsically un-doped polymers, possibly due to experimental difficulties arising from ion/charge injection barriers at large geometries. This highlights the need for new techniques and models. Furthermore, while the Cottrell equation has often been (mis)used to extract ion diffusivity from chronoamperometric measurements,[36,38] we would like to emphasize that the Cottrell equation does not account for the significant effect of RC charging in OMIEC films, thus leading to inaccurate ion mobility values. Moreover, the Cottrell equation assumes a surface-related redox reaction event, as opposed to the volumetric and often electrostatics-driven charge compensation in OMIECs.

Electrochemical strain microscopy (ESM)[40] and infrared photo-induced force microscopy (PiFM)[152] are two other methods that can be used to monitor ion motion in films. In ESM, an AC bias is applied to the AFM cantilever in contact with the polymer film immersed in an electrolyte, inducing local oxidation/reduction upon simultaneous ion injection/expulsion from the film (Fig. 7B). The local swelling/de-swelling is monitored as a function of the ESM amplitude.[93,153] Giridharagopal *et al.* first demonstrated this technique using poly(3-hexylthiophene-2,5-diyl) (P3HT) films.[40] The ESM images overlaid with stiffness pixels of P3HT revealed heterogeneous local swelling of the film under electrochemical doping, where morphology ranging from more amorphous (softer, Fig. 7C-i) to more crystalline (stiffer, Fig. 7C-ii) correlated with enhanced or diminished ion uptake, respectively. This work represents the first direct visualization of ion uptake-induced morphological changes. The ESM technique was later successfully applied by the same team to poly[2,5-(2-octyldodecyl)-3,6-diketopyrrolopyrrole-*alt*-5,5-(2,5-di(thien-2-yl)thieno[3,2-*b*]thiophene, DPP-DTT nanowires, showing volumetric electrochemical operation.[153] Overall, ESM represents a powerful technique to correlate nanoscale variations in ion uptake with morphological changes therein and polymer packing. However, this method is still vastly underused, possibly due to operational challenges.

PiFM allows monitoring of the IR signature of the ions injected into the films by measuring the IR-induced dipole–dipole interactions between the AFM probe tip and substrate (Fig. 7C). This technique was successfully applied to monitor the uptake of PF_6^- anion (by following the anion characteristic IR P–F stretch absorption peak) while mapping the film morphology of different dry polymers such as (poly[2,5-bis(thiophenyl)-1,4-bis(2-(2-(2-methoxyethoxy)ethoxy)ethoxy)benzene-PB2T-TEG, poly(3-((2-(2-methoxyethoxy)ethoxy)methyl)thiophene-2,5-diyl)-P3MEEMT, and DPP-DTT) and film architectures (thin films and nanowires).[30,152,153] When the nanowire film was electrochemically doped up to its half section, the PF_6^- ions did not show up in the topography but were very obvious in the PiFM image, indicating that the ions penetrated the matrix (Fig. 7C-i). Conversely, when the PF_6^- ions could not penetrate the bulk of the film, the ions were visible on the surface morphology, and the PF_6^- signal was observed uniformly on the surface (Fig. 7C-ii). PiFM can thus give valuable information on the spatial distribution of dopants (ions), allowing to map ion uptake distribution in crystalline and amorphous parts of the film.[30] However, PiFM requires vacuum conditions and, thus, does not reflect real-time ion injection into the film. Furthermore, its use for conjugated polymers has been restricted to p-type polymers, as there is yet to find a cation with a characteristic IR signature like PF_6^- for n-type materials ion uptake imaging.

Glow Discharge Optical Emission Spectroscopy (GDOES) is an analytical technique that provides quantitative measurements of the elemental depth profile of a substrate. GDOES was useful in investigating ionic charge depth distribution profiles within conjugated polymer films. Flagg *et al.* demonstrated through GDOES measurements that both ions from

1016 | *Chem. Soc. Rev.*, 2023, **52**, 1001–1023

This journal is © The Royal Society of Chemistry 2023

KPF_6 could diffuse within the P3MEEMT polymer film before electrochemical doping as opposed to $TBAPF_6$.[76] Conversely, none of the ions from the Cl^- based electrolytes could enter the film. Before electrochemical doping, the passive diffusion of the non-compensating ion within the film was considered responsible for the earlier oxidation onset. The oxidation of the films was hypothesized to occur first through cation expulsion, followed by the injection of the compensating anion from the electrolyte. Another technique that can be used to track ion distribution inside the film is Secondary Ion Mass Spectrometry (SIMS).[36] Despite its higher resolution, unlike GDOES, SIMS cannot be performed *in situ* and requires careful sample preparation to ensure that ions remain in the film upon doping.

3.4. Swelling

By measuring the capacitance of the film, we estimate the number of electrolyte ions compensating for the electronic charge carriers in the film. In the OECT configuration, this number corresponds to the ionic charge injected in the channel, which can be calculated from the integrated I_G measured over time. Under certain assumptions, another method can be used to calculate the number of electrolyte ions the film takes up during charging and any losses associated with the ionic–electronic charge coupling. This method is the quartz crystal microbalance with dissipation monitoring integrated with an electrochemistry module, *i.e.*, eQCM-D. QCM-D is a powerful tool leveraged to study mass changes observed on a film during adsorption or desorption processes.[154,155] The OMIEC film is coated on a quartz crystal where changes in its oscillation frequencies (Δf) and the concomitant energy dissipation (Δd) are monitored (Fig. 8A-i–ii) and subsequently translated into mass (or thickness) values. Decreased frequency is associated with increased mass of the coated sensor, and increased dissipation is associated with softening of the film (Fig. 8A-iv). Recording the sensor oscillation frequency at multiple overtones of the fundamental frequency gives information about the mass change at different vertical regions of the film,[156] as the penetration depth decreases with an increase in the overtone number. Higher overtone numbers are more sensitive to surface phenomena, while lower numbers relate more to the bulk.[157]

The challenging part of analyzing the gravimetric QCM-D data is choosing the appropriate model. Four models were developed for polymer thin films are the Sauerbrey model, the viscoelastic models (Voigt and extended Voigt), and the hydrodynamic model. Sauerbrey model relates Δf to the changes in the mass of the polymer (Δm) according to eqn (20):

$$\Delta m = -C\frac{\Delta f}{n} \qquad (20)$$

where C is the mass sensitivity constant of the sensor (-17.7 for a 5 MHz quartz sensor), and n is the overtone number. This model is appropriate when the film is rigid, displaying a small change in dissipation and low spreading of the overtones (Fig. 8B). A value of $|\Delta d_n/(\Delta f_n)|$ smaller than 4×10^{-7} Hz^{-1} was suggested to be the validity limit for this model.[158]

For a thicker or softer film that shows a large Δd and spreading of its overtones, the viscoelastic models are more appropriate (Fig. 8B). A Voigt (and extended Voigt) model characterizes materials that exhibit both elastic and viscous properties, as described in eqn (21):

$$G^\star = \mu + 2\pi i f\eta \qquad (21)$$

with $G^\star$ the complex shear modulus, μ the elasticity ($kg\ m^{-1}\ s^{-2}$), η the viscosity ($kg\ m^{-1}\ s^{-1}$), and f is the frequency. Here, using multiple overtones (minimum three, except the fundamental frequency) is a good practice to achieve a qualitative fit. For a more detailed overview of the QCM-D models, along with experimental guidelines, we refer the reader to a recent review by Easley *et al.*[154]

When coupled with a potentiostat, QCM-D can monitor the mass changes in the film during the application of a voltage while collecting electrical data (Fig. 8C). These mass changes reflect the changes the film undergoes during its interactions with electrolyte ions. Savva *et al.* used e-QCMD to investigate ion-to-electron coupling efficiency in a PEDOT:PSS film.[95] By correlating the mass changes observed during electrochemical doping/dedoping cycles to the concomitant charge measured, the authors found that more ions were injected into the film than the charges extracted. Assuming that each ion couples with one hole, the authors found that the ions entered the film by dragging water along them. However, the water that the film uptakes during electrochemical dedoping has not affected the performance of PEDOT:PSS OECTs as the films readily swell (up to double their initial weight) passively in the absence of biasing. Using eQCM-D, the authors revealed that a large amount of water is taken up by semiconducting films used in the channel of enhancement mode OECTs (Fig. 8D).[38,39,107,123] The excess water was shown to be detrimental to electronic charge transport, irreversibly changing the film morphology. The increase in hydration always enhanced ion transport by excess water but decreased charge mobility (Fig. 8D and E).[38] These studies showed that film swelling is an important property to characterize an OMIEC, and it should be optimized through chemical design or device operating conditions.

3.5. Theoretical approaches

While the techniques summarized in Sections 3.3 and 3.4 can provide important information about swelling and ion transport and diffusion in OMIEC films, a thorough understanding of the structure-property relationships and prediction of properties through chemical structure calls for theoretical approaches, such as molecular dynamics (MD) simulations. In such simulations, as opposed to traditional quantum mechanical treatment, the different properties of a material are investigated using force fields, which appropriately describe the averaged effect of the molecular electrons on the covalent bonding and van der Waals-type forces.[159] MD simulations have proven to be a powerful tool to understand polymer–electrolyte interactions, providing valuable information on (i) dynamic properties such as electrolyte diffusion, segmental
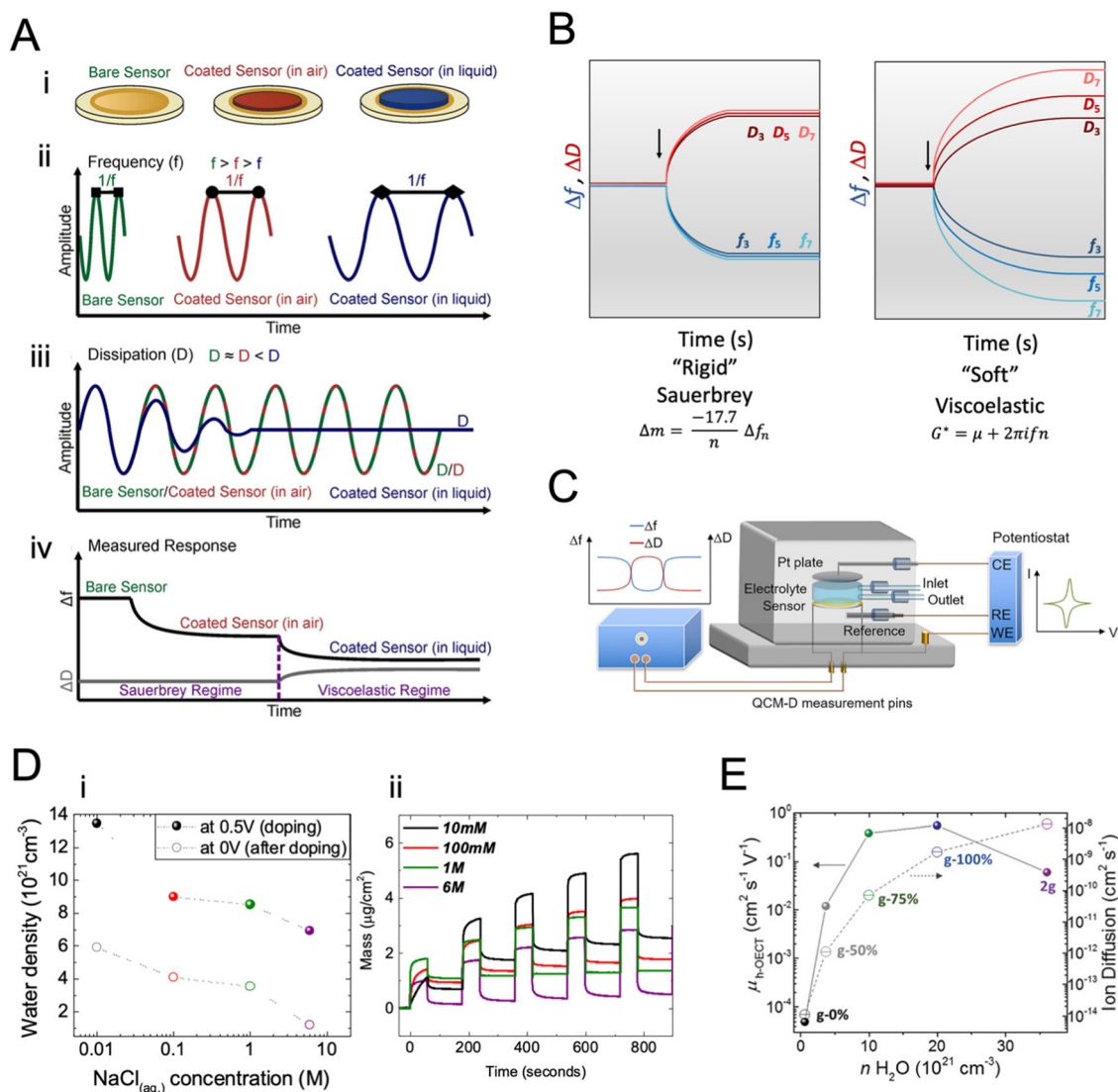
This journal is © The Royal Society of Chemistry 2023

Chem. Soc. Rev., 2023, **52**, 1001–1023 | **1017**

Fig. 8 Quartz crystal microbalance with dissipation monitoring, QCM-D. (A) (i): depictions of a bare QCM-D sensor, a thin polymer film-coated sensor in air, and a swollen polymer film-coated sensor in liquid. (ii) Qualitative frequency (Δf) and (iii) dissipation (ΔD) changes in sensor oscillations after polymer coating and changing the medium to liquid. (iv) A mock QCM-D response for the change in a single overtone Δf and ΔD with the Sauerbrey and viscoelastic model regimes identified. Adapted with permission from ref. 154. Copyright 2021 Wiley-VCH; (B) the signals are acquired at different overtones, here represented as f_n and D_n, respectively, with n = 3, 5, 7 for the 3rd, 5th, and 7th overtones. Depending on the material's nature, *i.e.*, rigid or soft, the Sauerbrey or viscoelastic models can be used to analyze the data; (C) schematic diagram of the e-QCMD set-up. The sensor mounted at the bottom serves as the working electrode; any changes happening at the surface in the electrochemical environment are measured in real-time by monitoring Δf and ΔD. The Pt ceiling acts as the counter electrode, and the reference electrode is mounted in the outlet flow close to the working electrode. Adapted with permission from ref. 154. Copyright 2021 Wiley-VCH. (D) (i) Changes in the mass of the films when doped in four electrolytes of varying ion concentrations. (ii) The number of water molecules injected into the films at the end of the doping pulse at 0.5 V and remaining in the film upon the subsequent dedoping pulse applied at 0 V as a function of NaCl concentration. Adapted with permission from ref. 38. Copyright 2019 American Chemical Society; (E) hole mobility of p-type OMIEC materials and ion diffusion coefficients as a function of the amount of water taken up by the polymers upon doping at 0.5 V *versus* V_{OC}. Adapted with permission from ref. 123. Copyright 2020 Wiley-VCH.

chain motion, and swelling and (ii) equilibrium properties such as aggregation, nonbonding interactions, and conformational features (side chain and backbone flexibility, electrolyte coordination).[155] Siemons *et al.* constructed an MD model to investigate the gradual exchange of hydrophobic alkyl-based side chains with hydrophilic EG-based side chains on polythiophenes.[160] The authors demonstrated that the oxygen content of the side chains influenced the packing behavior of the resulting OMIEC, where EG-based OMIEC was found to pack more effectively for charge transport in the solid state. Water was found to penetrate the OMIEC bulk through the π-stack (backbone) for the alkylated polymers and the lamellar stack (side chains) for the glycolated polymers. Further, the interactions of EG side chains with cations revealed the formation of a metastable single-bound state, or an energetically deep double-bound state, both with a strong side-chain length

1018 | *Chem. Soc. Rev.*, 2023, **52**, 1001–1023

This journal is © The Royal Society of Chemistry 2023

dependence. As such, (EG)$_3$ side chains were found to be optimal to ensure no cation trapping in the crystalline phase of OMIECs, while (EG)$_4$ should be preferred if such property is desired. Another study from the same team demonstrated the preferential interactions of ions with the donor (anions) or acceptor (cations) units of glycolated diketopyrrolopyrrole (DPP)-based copolymers and how the side chain nature could influence such interactions for maximized OECT performance.[161] Furthermore, MD simulations were successfully used to study phase transitions in OMIECs amorphous phase during electrochemical doping and ion injection,[162–164] despite relying on AMBER force field, a non-validated force field model for the systems investigated and generally used to model non-conjugated system.[165] To accurately model OMIECs, a possible alternative is to reparametrize backbone dihedral angles to capture more accurately the torsional behavior of the conjugated units. This was effectively used to investigate the effect of the EG side chain length on short-range intermolecular interactions and aggregation behavior of glycolated polythiophenes,[166] and to study how the anion nature can influence polymer–electrolyte interactions.[167] Lastly, more advanced models based on coarse-grained simulations have investigated the effect of side chain hydrophilicity on OMIEC morphology and charge transport,[168] water uptake and ion diffusion.[169,170]

4. Conclusion and outlook

In this review, we introduced the OECT technology and described the currently established operation mechanism and common fabrication techniques. We discussed the techniques used in the characterization of OECTs and the materials that render volumetric ionic (de)doping possible. We proposed guidelines to help report the main performance metrics of OECTs and OMIEC figures of merits for benchmarking emergent devices and mixed conductors. We emphasized the need to describe the device architecture (e.g., channel geometry, film thickness) and measurement conditions (e.g., scan rate, biasing conditions) when reporting device and materials characteristics. New OMIECs, with enhanced charge transport performance and tailored properties, are under continuous development to generate new device functionalities. With these guidelines, a consistent comparison of properties of new OMIECs and OECTs may be possible, which will help identify advances and opportunities to improve OMIEC molecular design. Note that the best-performing material in terms of mixed conductivity is not necessarily the best-suited material for a given application. For instance, while high operation stability and reversibility are important for biosensors, tunable and reversible hysteresis and structural changes are desirable for memory and neuromorphic devices.

The OECT transient and steady-state behavior was first described by Bernards and Malliaras who built the foundation of advanced and more accurate models. For instance, lateral motion of ions, contact resistance effects, and new interpretations of Bernard's model parameters have been proposed to refine our understanding of the device operation. Such models have allowed to operate devices at a faster speed through careful optimization of the biasing conditions and the device environment such as electrolyte nature. Device simulation and modeling is, therefore, very important to develop better devices and operating conditions for targeted applications.

Lastly, we would like to highlight the need for methods that can monitor ion transport, especially in intrinsically semi-conducting films which are doped by mobile ions. We have highlighted techniques that have been used, e.g., ESM and (e)QCM-D, to monitor ion uptake and release although each entails challenges in measurement conditions and analysis. Computational methods, such as MD and DFT calculations, are powerful tools that can assist in answering questions related to ion transport. We envision that combined operando characterization methods and the guidance of theoretical models of polymer/ion interactions will give important insights into materials design and enable researchers to find conditions to fine control and tune ion motion in OMIEC films.

Conflicts of interest

There are no conflicts to declare.

Acknowledgements

References

1 J. Rivnay, S. Inal, A. Salleo, R. M. Owens, M. Berggren and G. G. Malliaras, Nat. Rev. Mater., 2018, 3, 1–14.

2 S. Inal, G. G. Malliaras and J. Rivnay, Nat. Commun., 2017, 8, 1–7.

3 D. Khodagholy, T. Doublet, P. Quilichini, M. Gurfinkel, P. Leleux, A. Ghestem, E. Ismailova, T. Hervé, S. Sanaur and C. Bernard, Nat. Commun., 2013, 4, 1–7.

4 W. Lee, D. Kim, N. Matsuhisa, M. Nagase, M. Sekino, G. G. Malliaras, T. Yokota and T. Someya, Proc. Natl. Acad. Sci. U. S. A., 2017, 114, 10554–10559.

5 K. Xie, N. Wang, X. Lin, Z. Wang, X. Zhao, P. Fang, H. Yue, J. Kim, J. Luo and S. Cui, eLife, 2020, 9, e50345.

6 A. M. Pappa, D. Ohayon, A. Giovannitti, I. P. Maria, A. Savva, I. Uguz, J. Rivnay, I. McCulloch, R. M. Owens and S. Inal, Sci. Adv., 2018, 4, eaat0911.

7 D. Ohayon, G. Nikiforidis, A. Savva, A. Giugni, S. Wustoni, T. Palanisamy, X. Chen, I. P. Maria, E. Di Fabrizio and P. M. Costa, Nat. Mater., 2020, 19, 456–463.

8 S. Wustoni, T. C. Hidalgo, A. Hama, D. Ohayon, A. Savva, N. Wei, N. Wehbe and S. Inal, Adv. Mater. Technol., 2020, 5, 1900943.

9 A. M. Pappa, V. F. Curto, M. Braendlein, X. Strakosas, M. J. Donahue, M. Fiocchi, G. G. Malliaras and R. M. Owens, *Adv. Healthcare Mater.*, 2016, **5**, 2295–2302.

10 L. J. Currano, F. C. Sage, M. Hagedon, L. Hamilton, J. Patrone and K. Gerasopoulos, *Sci. Rep.*, 2018, **8**, 1–11.

11 M. Braendlein, A. M. Pappa, M. Ferro, A. Lopresti, C. Acquaviva, E. Mamessier, G. G. Malliaras and R. M. Owens, *Adv. Mater.*, 2017, **29**, 1605744.

12 C. Diacci, T. Abedi, J. W. Lee, E. O. Gabrielsson, M. Berggren, D. T. Simon, T. Niittylä and E. Stavrinidou, *Iscience*, 2021, **24**, 101966.

13 A. Koklu, D. Ohayon, S. Wustoni, A. Hama, X. Chen, I. McCulloch and S. Inal, *Sens. Actuators, B*, 2021, **329**, 129251.

14 K. Guo, S. Wustoni, A. Koklu, E. Díaz-Galicia, M. Moser, A. Hama, A. A. Alqahtani, A. N. Ahmad, F. S. Alhamlan and M. Shuaib, *Nat. Biomed. Eng.*, 2021, **5**, 666–677.

15 H. Liu, A. Yang, J. Song, N. Wang, P. Lam, Y. Li, H. K.-W. Law and F. Yan, *Sci. Adv.*, 2021, **7**, eabg8387.

16 L. H. Jimison, S. A. Tria, D. Khodagholy, M. Gurfinkel, E. Lanzarini, A. Hama, G. G. Malliaras and R. M. Owens, *Adv. Mater.*, 2012, **24**, 5919–5923.

17 F. Decataldo, M. Barbalinardo, M. Tessarolo, V. Vurro, M. Calienni, D. Gentili, F. Valle, M. Cavallini and B. Fraboni, *Adv. Mater. Technol.*, 2019, **4**, 1900207.

18 P. Cavassin, A. M. Pappa, C. Pitsalidis, H. F. P. Barbosa, R. Colucci, J. Saez, Y. Tuchman, A. Salleo, G. C. Faria and R. M. Owens, *Adv. Mater. Technol.*, 2020, **5**, 1900680.

19 A.-M. Pappa, H.-Y. Liu, W. Traberg-Christensen, Q. Thiburce, A. Savva, A. Pavia, A. Salleo, S. Daniel and R. M. Owens, *ACS Nano*, 2020, **14**, 12538–12545.

20 M. Kawan, T. C. Hidalgo, W. Du, A.-M. Pappa, R. M. Owens, I. McCulloch and S. Inal, *Mater. Horiz.*, 2020, **7**, 2348–2358.

21 S. Chen, A. Surendran, X. Wu and W. L. Leong, *Adv. Funct. Mater.*, 2020, **30**, 2006186.

22 B. D. Paulsen, K. Tybrandt, E. Stavrinidou and J. Rivnay, *Nat. Mater.*, 2020, **19**, 13–26.

23 C. J. Kousseff, R. Halaksa, Z. S. Parr and C. B. Nielsen, *Chem. Rev.*, 2021, **122**, 4397–4419.

24 D. Tu and S. Fabiano, *Appl. Phys. Lett.*, 2020, **117**, 080501.

25 J. Rivnay, S. Inal, B. A. Collins, M. Sessolo, E. Stavrinidou, X. Strakosas, C. Tassone, D. M. Delongchamp and G. G. Malliaras, *Nat. Commun.*, 2016, **7**, 1–9.

26 H. Y. Wu, C. Y. Yang, Q. Li, N. B. Kolhe, X. Strakosas, M. A. Stoeckel, Z. Wu, W. Jin, M. Savvakis and R. Kroon, *Adv. Mater.*, 2022, **34**, 2106235.

27 A. Giovannitti, D.-T. Sbircea, S. Inal, C. B. Nielsen, E. Bandiello, D. A. Hanifi, M. Sessolo, G. G. Malliaras, I. McCulloch and J. Rivnay, *Proc. Natl. Acad. Sci. U. S. A.*, 2016, **113**, 12017–12022.

28 A. Giovannitti, I. P. Maria, D. Hanifi, M. J. Donahue, D. Bryant, K. J. Barth, B. E. Makdah, A. Savva, D. Moia and M. S. Zetek, *Chem. Mater.*, 2018, **30**, 2945–2953.

29 J. F. Ponder Jr, S. A. Gregory, A. Atassi, A. K. Menon, A. W. Lang, L. R. Savagian, J. R. Reynolds and S. K. Yee, *J. Am. Chem. Soc.*, 2022, **144**, 1351–1360.

30 L. Q. Flagg, C. G. Bischak, J. W. Onorato, R. B. Rashid, C. K. Luscombe and D. S. Ginger, *J. Am. Chem. Soc.*, 2019, **141**, 4345–4354.

31 N. Kim, S. Kee, S. H. Lee, B. H. Lee, Y. H. Kahng, Y. R. Jo, B. J. Kim and K. Lee, *Adv. Mater.*, 2014, **26**, 2268–2272.

32 A. Savva, D. Ohayon, J. Surgailis, A. F. Paterson, T. C. Hidalgo, X. Chen, I. P. Maria, B. D. Paulsen, A. J. Petty and J. Rivnay, *Adv. Electron. Mater.*, 2019, **5**, 1900249.

33 L. V. Lingstedt, M. Ghittorelli, H. Lu, D. A. Koutsouras, T. Marszalek, F. Torricelli, N. I. Crăciun, P. Gkoupidenis and P. W. Blom, *Adv. Electron. Mater.*, 2019, **5**, 1800804.

34 J. Nightingale, C. Pitsalidis, A.-M. Pappa, E. Tan, K. Stewart, R. M. Owens and J.-S. Kim, *J. Mater. Chem. C*, 2020, **8**, 8846–8855.

35 T. C. Hidalgo Castillo, M. Moser, C. Cendra, P. D. Nayak, A. Salleo, I. McCulloch and S. Inal, *Chem. Mater.*, 2022, **34**, 6723–6733.

36 A. F. Paterson, A. Savva, S. Wustoni, L. Tsetseris, B. D. Paulsen, H. Faber, A. H. Emwas, X. Chen, G. Nikiforidis and T. C. Hidalgo, *Nat. Commun.*, 2020, **11**, 1–11.

37 S. T. M. Tan, G. Lee, I. Denti, G. LeCroy, K. Rozylowicz, A. Marks, S. Griggs, I. McCulloch, A. Giovannitti and A. Salleo, *Adv. Mater.*, 2022, **34**, 2202359.

38 A. Savva, C. Cendra, A. Giugni, B. Torre, J. Surgailis, D. Ohayon, A. Giovannitti, I. McCulloch, E. Di Fabrizio and A. Salleo, *Chem. Mater.*, 2019, **31**, 927–937.

39 J. Surgailis, A. Savva, V. Druet, B. D. Paulsen, R. Wu, A. Hamidi-Sakr, D. Ohayon, G. Nikiforidis, X. Chen and I. McCulloch, *Adv. Funct. Mater.*, 2021, 2010165.

40 R. Giridharagopal, L. Flagg, J. Harrison, M. Ziffer, J. Onorato, C. Luscombe and D. Ginger, *Nat. Mater.*, 2017, **16**, 737–742.

41 A. Koklu, D. Ohayon, S. Wustoni, V. Druet, A. Saleh and S. Inal, *Chem. Rev.*, 2021, **122**, 4581–4635.

42 Z. Li, J. Hu, G. Gao, X.-N. Liu, J.-Q. Wu, Y.-T. Xu, H. Zhou, W.-W. Zhao, J.-J. Xu and H.-Y. Chen, *Sens. Diagn.*, 2022, **1**, 294–300.

43 M.-J. Lu, F.-Z. Chen, J. Hu, H. Zhou, G. Chen, X.-D. Yu, R. Ban, P. Lin and W.-W. Zhao, *Small Struct.*, 2021, **2**, 2100087.

44 C. Liao, M. Zhang, L. Niu, Z. Zheng and F. Yan, *J. Mater. Chem. B*, 2014, **2**, 191–200.

45 C. Peruzzi, S. Battistoni, D. Montesarchio, M. Cocuzza, S. L. Marasso, A. Verna, L. Pasquardini, R. Verucchi, L. Aversa and V. Erokhin, *Sci. Rep.*, 2021, **11**, 1–11.

46 D. A. Koutsouras, K. Lieberth, F. Torricelli, P. Gkoupidenis and P. W. Blom, *Adv. Mater. Technol.*, 2021, **6**, 2100591.

47 M. Giordani, M. Berto, M. Di Lauro, C. A. Bortolotti, M. Zoli and F. Biscarini, *ACS Sens.*, 2017, **2**, 1756–1760.

48 A. Williamson, M. Ferro, P. Leleux, E. Ismailova, A. Kaszas, T. Doublet, P. Quilichini, J. Rivnay, B. Rózsa and G. Katona, *Adv. Mater.*, 2015, **27**, 4405–4410.

49 Y. J. Jo, K. Y. Kwon, Z. U. Khan, X. Crispin and T.-I. Kim, *ACS Appl. Mater. Interfaces*, 2018, **10**, 39083–39090.

50 H. Lee, S. Lee, W. Lee, T. Yokota, K. Fukuda and T. Someya, *Adv. Funct. Mater.*, 2019, **29**, 1906982.

1020 | *Chem. Soc. Rev.*, 2023, **52**, 1001–1023

This journal is © The Royal Society of Chemistry 2023

51 P. R. Paudel, D. Dahal, R. K. Radha Krishnan, M. Skowrons and B. Lüssem, *AIP Adv.*, 2022, **12**, 045310.

52 P. A. Ersman, D. Westerberg, D. Tu, M. Nilsson, J. Åhlin, A. Eveborn, A. Lagerlöf, D. Nilsson, M. Sandberg and P. Norberg, *Flexible Printed Electron.*, 2017, **2**, 045008.

53 S. T. Keene, D. Fogarty, R. Cooke, C. D. Casadevall, A. Salleo and O. Parlak, *Adv. Healthcare Mater.*, 2019, **8**, 1901321.

54 M. J. Donahue, A. Williamson, X. Strakosas, J. T. Friedlein, R. R. McLeod, H. Gleskova and G. G. Malliaras, *Adv. Mater.*, 2018, **30**, 1705031.

55 A. G. Polyravas, V. F. Curto, N. Schaefer, A. B. Calia, A. Guimera-Brunet, J. A. Garrido and G. G. Malliaras, *Flexible Printed Electron.*, 2019, **4**, 044003.

56 A. F. Paterson, H. Faber, A. Savva, G. Nikiforidis, M. Gedda, T. C. Hidalgo, X. Chen, I. McCulloch, T. D. Anthopoulos and S. Inal, *Adv. Mater.*, 2019, **31**, 1902291.

57 A. R. Hassan, Z. Zhao, J. J. Ferrero, C. Cea, J. Pastrzebska-Perfect, J. Myers, P. Asman, N. F. Ince, G. McKhann and A. Viswanathan, *Adv. Sci.*, 2022, 2202306.

58 S. Park, S. W. Heo, W. Lee, D. Inoue, Z. Jiang, K. Yu, H. Jinno, D. Hashizume, M. Sekino and T. Yokota, *Nature*, 2018, **561**, 516–521.

59 L. Basiricò, P. Cosseddu, A. Scidà, B. Fraboni, G. Malliaras and A. Bonfiglio, *Org. Electron.*, 2012, **13**, 244–248.

60 H. Sirringhaus, T. Kawase, R. Friend, T. Shimoda, M. Inbasekaran, W. Wu and E. Woo, *Science*, 2000, **290**, 2123–2126.

61 R. R. Søndergaard, M. Hösel and F. C. Krebs, *J. Polym. Sci., Part B: Polym. Phys.*, 2013, **51**, 16–34.

62 E. Bihar, Y. Deng, T. Miyake, M. Saadaoui, G. G. Malliaras and M. Rolandi, *Sci. Rep.*, 2016, **6**, 1–6.

63 T. N. Mangoma, S. Yamamoto, G. G. Malliaras and R. Daly, *Adv. Mater. Technol.*, 2022, **7**, 2000798.

64 M. Zabihipour, R. Lassnig, J. Strandberg, M. Berggren, S. Fabiano, I. Engquist and P. Andersson Ersman, *npj Flexible Electron.*, 2020, **4**, 1–8.

65 M. Nishinaka, H. Jinno, Y. Jimbo, S. Lee, J. Wang, W. Lee, T. Yokota and T. Someya, *Small Struct.*, 2021, **2**, 2000088.

66 X. Wu, A. Surendran, M. Moser, S. Chen, B. T. Muhammad, I. P. Maria, I. McCulloch and W. L. Leong, *ACS Appl. Mater. Interfaces*, 2020, **12**, 20757–20764.

67 V. Bertana, G. Scordo, M. Parmeggiani, L. Scaltrito, S. Ferrero, M. G. Gomez, M. Cocuzza, D. Vurro, P. D'Angelo and S. Iannotta, *Sci. Rep.*, 2020, **10**, 1–11.

68 H. Ma, Y. Chen, X. Li and B. Li, *Adv. Funct. Mater.*, 2021, **31**, 2101861.

69 E. V. Canesi, A. Luzio, B. Saglio, A. Bianco, M. Caironi and C. Bertarelli, *ACS Macro Lett.*, 2012, **1**, 366–369.

70 J. Schoeller, F. Itel, K. Wuertz-Kozak, G. Fortunato and R. M. Rossi, *Polym. Rev.*, 2021, 1–49.

71 C. Pitsalidis, M. Ferro, D. Iandolo, L. Tzounis, S. Inal and R. Owens, *Sci. Adv.*, 2018, **4**, eaat4253.

72 C. M. Moysidou, C. Pitsalidis, M. Al-Sharabi, A. M. Withers, J. A. Zeitler and R. M. Owens, *Adv. Biol.*, 2021, **5**, 2000306.

73 X. Wu, J. Feng, J. Deng, Z. Cui, L. Wang, S. Xie, C. Chen, C. Tang, Z. Han and H. Yu, *Sci. China: Chem.*, 2020, **63**, 1281–1288.

74 S. K. Lee, Y. W. Cho, J. S. Lee, Y. R. Jung, S. H. Oh, J. Y. Sun, S. Kim and Y. C. Joo, *Adv. Sci.*, 2021, **8**, 2001544.

75 A. Yang, Y. Li, C. Yang, Y. Fu, N. Wang, L. Li and F. Yan, *Adv. Mater.*, 2018, **30**, 1800051.

76 L. Q. Flagg, C. G. Bischak, R. J. Quezada, J. W. Onorato, C. K. Luscombe and D. S. Ginger, *ACS Mater. Lett.*, 2020, **2**, 254–260.

77 P. Schmode, D. Ohayon, P. M. Reichstein, A. Savva, S. Inal and M. Thelakkat, *Chem. Mater.*, 2019, **31**, 5286–5295.

78 Y. Xuan, M. Sandberg, M. Berggren and X. Crispin, *Org. Electron.*, 2012, **13**, 632–637.

79 T. P. van der Pol, S. T. Keene, B. W. Saes, S. C. Meskers, A. Salleo, Y. van de Burgt and R. A. Janssen, *J. Phys. Chem. C*, 2019, **123**, 24328–24337.

80 I. Cruz-Cruz, M. Reyes-Reyes, I. A. Rosales-Gallegos, A. Y. Gorbatchev, J. M. Flores-Camacho and R. N. López-Sandoval, *J. Phys. Chem. C*, 2015, **119**, 19305–19311.

81 H. Sun, M. Vagin, S. Wang, X. Crispin, R. Forchheimer, M. Berggren and S. Fabiano, *Adv. Mater.*, 2018, **30**, 1704916.

82 C.-Y. Yang, M.-A. Stoeckel, T.-P. Ruoko, H.-Y. Wu, X. Liu, N. B. Kolhe, Z. Wu, Y. Puttisong, C. Musumeci and M. Massetti, *Nat. Commun.*, 2021, **12**, 1–8.

83 S. Zhang, M. Massetti, T. P. Ruoko, D. Tu, C. Y. Yang, X. Liu, Z. Wu, Y. Lee, R. Kroon and P. O. Persson, *Adv. Funct. Mater.*, 2022, **32**, 2106447.

84 P. Romele, P. Gkoupidenis, D. A. Koutsouras, K. Lieberth, Z. M. Kovács-Vajna, P. W. Blom and F. Torricelli, *Nat. Commun.*, 2020, **11**, 1–11.

85 P. C. Harikesh, C.-Y. Yang, D. Tu, J. Y. Gerasimov, A. M. Dar, A. Armada-Moreira, M. Massetti, R. Kroon, D. Bliman and R. Olsson, *Nat. Commun.*, 2022, **13**, 1–9.

86 X. Wu, T. L. D. Tam, S. Chen, T. Salim, X. Zhao, Z. Zhou, M. Lin, J. Xu, Y. L. Loo and W. L. Leong, *Adv. Mater.*, 2022, 2206118.

87 L. Travaglini, A. P. Micolich, C. Cazorla, E. Zeglio, A. Lauto and D. Mawad, *Adv. Funct. Mater.*, 2021, **31**, 2007205.

88 D. A. Bernards and G. G. Malliaras, *Adv. Funct. Mater.*, 2007, **17**, 3538–3544.

89 A. V. Volkov, K. Wijeratne, E. Mitraka, U. Ail, D. Zhao, K. Tybrandt, J. W. Andreasen, M. Berggren, X. Crispin and I. V. Zozoulenko, *Adv. Funct. Mater.*, 2017, **27**, 1700329.

90 J. T. Friedlein, R. R. McLeod and J. Rivnay, *Org. Electron.*, 2018, **63**, 398–414.

91 J. Rivnay, P. Leleux, M. Ferro, M. Sessolo, A. Williamson, D. A. Koutsouras, D. Khodagholy, M. Ramuz, X. Strakosas and R. M. Owens, *Sci. Adv.*, 2015, **1**, e1400251.

92 P. R. Paudel, V. Kaphle, D. Dahal, R. K. Radha Krishnan and B. Lüssem, *Adv. Funct. Mater.*, 2021, **31**, 2004939.

93 L. Q. Flagg, R. Giridharagopal, J. Guo and D. S. Ginger, *Chem. Mater.*, 2018, **30**, 5380–5389.

94 C. Cendra, A. Giovannitti, A. Savva, V. Venkatraman, I. McCulloch, A. Salleo, S. Inal and J. Rivnay, *Adv. Funct. Mater.*, 2019, **29**, 1807034.

This journal is © The Royal Society of Chemistry 2023

Chem. Soc. Rev., 2023, **52**, 1001–1023 | 1021

95 A. Savva, S. Wustoni and S. Inal, *J. Mater. Chem. C*, 2018, **6**, 12023–12030.

96 F. Cicoira, M. Sessolo, O. Yaghmazadeh, J. A. DeFranco, S. Y. Yang and G. G. Malliaras, *Adv. Mater.*, 2010, **22**, 1012–1016.

97 G. Tarabella, C. Santato, S. Y. Yang, S. Iannotta, G. G. Malliaras and F. Cicoira, *Appl. Phys. Lett.*, 2010, **97**, 205.

98 J. T. Friedlein, M. J. Donahue, S. E. Shaheen, G. G. Malliaras and R. R. McLeod, *Adv. Mater.*, 2016, **28**, 8398–8404.

99 D. Nilsson, T. Kugler, P.-O. Svensson and M. Berggren, *Sens. Actuators, B*, 2002, **86**, 193–197.

100 A. Ortiz-Conde, F. G. Sánchez, J. J. Liou, A. Cerdeira, M. Estrada and Y. Yue, *Microelectron. Reliab.*, 2002, **42**, 583–596.

101 V. Kumar Singh and B. Mazhari, *Appl. Phys. Lett.*, 2013, **102**, 112_111.

102 J. Zaumseil and H. Sirringhaus, *Chem. Rev.*, 2007, **107**, 1296–1323.

103 R. Colucci, H. F. de Paula Barbosa, F. Günther, P. Cavassin and G. C. Faria, *Flexible Printed Electron.*, 2020, **5**, 013001.

104 P. Romele, M. Ghittorelli, Z. M. Kovács-Vajna and F. Torricelli, *Nat. Commun.*, 2019, **10**, 1–11.

105 S. E. Doris, A. Pierre and R. A. Street, *Adv. Mater.*, 2018, **30**, 1706757.

106 M. Sensi, M. Berto, A. Candini, A. Liscio, A. Cossarizza, V. Beni, F. Biscarini and C. A. Bortolotti, *ACS Omega*, 2019, **4**, 5374–5381.

107 P. Schmode, A. Savva, R. Kahl, D. Ohayon, F. Meichsner, O. Dolynchuk, T. Thurn-Albrecht, S. Inal and M. Thelakkat, *ACS Appl. Mater. Interfaces*, 2020, **12**, 13029–13039.

108 Y. Zhang, J. Li, R. Li, D.-T. Sbircea, A. Giovannitti, J. Xu, H. Xu, G. Zhou, L. Bian and I. McCulloch, *ACS Appl. Mater. Interfaces*, 2017, **9**, 38687–38694.

109 J. Ji, H. Wang, R. Liu, X. Jiang, Q. Zhang, Y. Peng, S. Sang, Q. Sun and Z. L. Wang, *Nano Energy*, 2021, **87**, 106116.

110 J. Rivnay, P. Leleux, M. Sessolo, D. Khodagholy, T. Hervé, M. Fiocchi and G. G. Malliaras, *Adv. Mater.*, 2013, **25**, 7010–7014.

111 A. Koklu, S. Wustoni, V.-E. Musteata, D. Ohayon, M. Moser, I. McCulloch, S. P. Nunes and S. Inal, *ACS Nano*, 2021, **15**, 8130–8141.

112 D. Khodagholy, J. Rivnay, M. Sessolo, M. Gurfinkel, P. Leleux, L. H. Jimison, E. Stavrinidou, T. Herve, S. Sanaur and R. M. Owens, *Nat. Commun.*, 2013, **4**, 1–6.

113 D. A. Koutsouras, P. Gkoupidenis, C. Stolz, V. Subramanian, G. G. Malliaras and D. C. Martin, *ChemElectroChem*, 2017, **4**, 2321–2327.

114 D. Ohayon, A. Savva, W. Du, B. D. Paulsen, I. Uguz, R. S. Ashraf, J. Rivnay, I. McCulloch and S. Inal, *ACS Appl. Mater. Interfaces*, 2021, **13**, 4253–4266.

115 N. Wang, Y. Liu, Y. Fu and F. Yan, *ACS Appl. Mater. Interfaces*, 2017, **10**, 25834–25840.

116 G. C. Faria, D. T. Duong and A. Salleo, *Org. Electron.*, 2017, **45**, 215–221.

117 Y. Zhong, A. Saleh and S. Inal, *Macromol. Biosci.*, 2021, **21**, 2100187.

118 J. Rivnay, M. Ramuz, P. Leleux, A. Hama, M. Huerta and R. M. Owens, *Appl. Phys. Lett.*, 2015, **106**, 8_1.

119 R. B. Rashid, W. Du, S. Griggs, I. P. Maria, I. McCulloch and J. Rivnay, *Sci. Adv.*, 2021, **7**, eabh1055.

120 G. D. Spyropoulos, J. N. Gelinas and D. Khodagholy, *Sci. Adv.*, 2019, **5**, eaau7378.

121 N. A. Kukhta, A. Marks and C. K. Luscombe, *Chem. Rev.*, 2021, **122**, 4325–4355.

122 S. E. Chen, L. Q. Flagg, J. W. Onorato, L. J. Richter, J. Guo, C. K. Luscombe and D. S. Ginger, *J. Mater. Chem. A*, 2022, **10**, 10738–10749.

123 A. Savva, R. Hallani, C. Cendra, J. Surgailis, T. C. Hidalgo, S. Wustoni, R. Sheelamanthula, X. Chen, M. Kirkus and A. Giovannitti, *Adv. Funct. Mater.*, 2020, **30**, 1907657.

124 J. T. Friedlein, S. E. Shaheen, G. G. Malliaras and R. R. McLeod, *Adv. Electron. Mater.*, 2015, **1**, 1500189.

125 F. Gentile, D. Delmonte, M. Solzi, M. Villani, S. Iannotta, A. Zappettini and N. Coppedè, *Org. Electron.*, 2016, **35**, 59–64.

126 M. Berggren, X. Crispin, S. Fabiano, M. P. Jonsson, D. T. Simon, E. Stavrinidou, K. Tybrandt and I. Zozoulenko, *Adv. Mater.*, 2019, **31**, 1805813.

127 P. R. Paudel, J. Tropp, V. Kaphle, J. D. Azoulay and B. Lüssem, *J. Mater. Chem. C*, 2021, **9**, 9761–9790.

128 N. Elgrishi, K. J. Rountree, B. D. McCarthy, E. S. Rountree, T. T. Eisenhart and J. L. Dempsey, *J. Chem. Educ.*, 2018, **95**, 197–206.

129 P. D'Angelo, S. L. Marasso, A. Verna, A. Ballesio, M. Parmeggiani, A. Sanginario, G. Tarabella, D. Demarchi, C. F. Pirri and M. Cocuzza, *Small*, 2019, **15**, 1902332.

130 G. Nikiforidis, S. Wustoni, D. Ohayon, V. Druet and S. Inal, *ACS Appl. Energy Mater.*, 2020, **3**, 7896–7907.

131 E. Stavrinidou, M. Sessolo, B. Winther-Jensen, S. Sanaur and G. G. Malliaras, *AIP Adv.*, 2014, **4**, 017127.

132 C. M. Proctor, J. Rivnay and G. G. Malliaras, *Journal*, 2016, **54**, 1433–1436.

133 M. Berggren and G. G. Malliaras, *Science*, 2019, **364**, 233–234.

134 E. Stavrinidou, P. Leleux, H. Rajaona, D. Khodagholy, J. Rivnay, M. Lindau, S. Sanaur and G. G. Malliaras, *Adv. Mater.*, 2013, **25**, 4488–4493.

135 C. Musumeci, M. Vagin, E. Zeglio, L. Ouyang, R. Gabrielsson and O. Inganäs, *J. Mater. Chem. C*, 2019, **7**, 2987–2993.

136 E. Barsoukov and J. R. Macdonald, *Applications*, John Wiley &Sons, Inc., Hoboken, NJ, 2nd edn, 2005.

137 A. M. Österholm, J. F. Ponder Jr, M. De Keersmaecker, D. E. Shen and J. R. Reynolds, *Chem. Mater.*, 2019, **31**, 2971–2982.

138 B. Ulgut, J. E. Grose, Y. Kiya, D. C. Ralph and H. D. Abruna, *Appl. Surf. Sci.*, 2009, **256**, 1304–1308.

139 H. H. Choi, K. Cho, C. D. Frisbie, H. Sirringhaus and V. Podzorov, *Nat. Mater.*, 2018, **17**, 2–7.

140 Y. Xu, Y. Li, S. Li, F. Balestra, G. Ghibaudo, W. Li, Y. F. Lin, H. Sun, J. Wan and X. Wang, *Adv. Funct. Mater.*, 2020, **30**, 1904508.

1022 | *Chem. Soc. Rev.*, 2023, **52**, 1001-1023

This journal is © The Royal Society of Chemistry 2023

141 F. Bonafè, F. Decataldo, B. Fraboni and T. Cramer, *Adv. Electron. Mater.*, 2021, **7**, 2100086.

142 L. J. van der Pauw, *Philips Tech. Rev.*, 1958, **20**, 220–224.

143 R. K. Hallani, B. D. Paulsen, A. J. Petty, R. Sheelamanthula, M. Moser, K. J. Thorley, W. Sohn, R. B. Rashid, A. Savva and S. Moro, *J. Am. Chem. Soc.*, 2021, **143**, 11007–11018.

144 X. Chen, A. Marks, B. D. Paulsen, R. Wu, R. B. Rashid, H. Chen, M. Alsufyani, J. Rivnay and I. McCulloch, *Angew., Chem., Int. Ed.*, 2021, **60**, 9368–9373.

145 Y. Kim, H. Noh, B. D. Paulsen, J. Kim, I. Y. Jo, H. Ahn, J. Rivnay and M. H. Yoon, *Adv. Mater.*, 2021, **33**, 2007550.

146 F. Mariani, F. Conzuelo, T. Cramer, I. Gualandi, L. Possanzini, M. Tessarolo, B. Fraboni, W. Schuhmann and E. Scavetta, *Small*, 2019, **15**, 1902534.

147 B. D. Paulsen and C. D. Frisbie, *J. Phys. Chem. C*, 2012, **116**, 3132–3141.

148 B. X. Dong, C. Nowak, J. W. Onorato, J. Strzalka, F. A. Escobedo, C. K. Luscombe, P. F. Nealey and S. N. Patel, *Chem. Mater.*, 2019, **31**, 1418–1429.

149 S. Inal, G. G. Malliaras and J. Rivnay, *J. Mater. Chem. C*, 2016, **4**, 3942–3947.

150 X. Wang, B. Shapiro and E. Smela, *J. Phys. Chem. C*, 2009, **113**, 382–401.

151 E. Stavrinidou, P. Leleux, H. Rajaona, M. Fiocchi, S. Sanaur and G. G. Malliaras, *J. Appl. Phys.*, 2013, **113**, 244501.

152 C. G. Bischak, L. Q. Flagg, K. Yan, T. Rehman, D. W. Davies, R. J. Quezada, J. W. Onorato, C. K. Luscombe, Y. Diao and C.-Z. Li, *J. Am. Chem. Soc.*, 2020, **142**, 7434–7442.

153 R. Giridharagopal, J. Guo, J. Kong and D. S. Ginger, *ACS Appl. Mater. Interfaces*, 2021, **13**, 34616–34624.

154 A. D. Easley, T. Ma, C. I. Eneh, J. Yun, R. M. Thakur and J. L. Lutkenhaus, *J. Polym. Sci.*, 2021, **60**, 1090.

155 R. Wu, M. Matta, B. D. Paulsen and J. Rivnay, *Chem. Rev.*, 2022, **122**, 4493–4551.

156 L. A. Galuska, E. S. Muckley, Z. Cao, D. F. Ehlenberg, Z. Qian, S. Zhang, S. Rondeau-Gagné, M. D. Phan, J. F. Ankner and I. N. Ivanov, *Nat. Commun.*, 2021, **12**, 1–11.

157 K. Singh and C. F. Blanford, *ChemCatChem*, 2014, **6**, 921–929.

158 I. Reviakine, D. Johannsmann and R. P. Richter, *Anal. Chem.*, 2011, **83**, 8838–8848.

159 J. Wildman, P. Repiščák, M. J. Paterson and I. Galbraith, *J. Chem. Theory Comput.*, 2016, **12**, 3813–3824.

160 N. Siemons, D. Pearce, C. Cendra, H. Yu, S. M. Tuladhar, R. K. Hallani, R. Sheelamanthula, G. S. LeCroy, L. Siemons, A. J. White, I. McCulloch, A. Salleo, J. M. Frost, A. Giovannitti and J. Nelson, *Adv. Mater.*, 2022, **34**, 2204258.

161 E. Tan, J. Kim, K. Stewart, C. Pitsalidis, S. Kwon, N. Siemons, J. Kim, Y. Jiang, J. M. Frost and D. Pearce, *Adv. Mater.*, 2022, 2202574.

162 S. Ghosh and I. Zozoulenko, *ACS Appl. Electron. Mater.*, 2020, **2**, 4034–4041.

163 J. Gladisch, E. Stavrinidou, S. Ghosh, A. Giovannitti, M. Moser, I. Zozoulenko, I. McCulloch and M. Berggren, *Adv. Sci.*, 2020, **7**, 1901144.

164 M. Moser, J. Gladisch, S. Ghosh, T. C. Hidalgo, J. F. Ponder Jr, R. Sheelamanthula, Q. Thiburce, N. Gasparini, A. Wadsworth and A. Salleo, *Adv. Funct. Mater.*, 2021, **31**, 2100723.

165 K. H. DuBay, M. L. Hall, T. F. Hughes, C. Wu, D. R. Reichman and R. A. Friesner, *J. Chem. Theory Comput.*, 2012, **8**, 4556–4569.

166 M. Moser, L. R. Savagian, A. Savva, M. Matta, J. F. Ponder Jr, T. C. Hidalgo, D. Ohayon, R. Hallani, M. Reisjalali and A. Troisi, *Chem. Mater.*, 2020, **32**, 6618–6628.

167 M. Matta, R. Wu, B. D. Paulsen, A. J. Petty, R. Sheelamanthula, I. McCulloch, G. C. Schatz and J. Rivnay, *Chem. Mater.*, 2020, **32**, 7301–7308.

168 A. Khot and B. M. Savoie, *J. Polym. Sci.*, 2022, **60**, 610–620.

169 N. Delavari, J. Gladisch, I. Petsagkourakis, X. Liu, M. Modarresi, M. Fahlman, E. Stavrinidou, M. Linares and I. Zozoulenko, *Macromolecules*, 2021, **54**, 6552–6562.

170 M. Modarresi, J. F. Franco-Gonzalez and I. Zozoulenko, *Phys. Chem. Chem. Phys.*, 2018, **20**, 17188–17198.

This journal is © The Royal Society of Chemistry 2023

Chem. Soc. Rev., 2023, **52**, 1001–1023 | 1023